

FINAL TECHNICAL REPORT

NASA grant NAG5-7643

XTE proposal #20102—"SS 433's High Energy Spectrum"

David L. Band

September 30, 1999

This grant supported a set of *RXTE* observations of SS433, one of three sets of observations we have performed thus far. SS 433 is a jet-producing compact binary system which is an analogue of extragalactic active galactic as well as a fascinating endpoint of stellar evolution. We have analyzed the *RXTE* observations and prepared a draft paper which is appended. Publication of this paper will be supported by other funds. The *RXTE* observations were contemporaneous with observations by other instruments, and cross-comparisons are in progress. Because we are analyzing observations from the first three *RXTE* observations, we discuss the results from all three here.

The *RXTE* observations of SS 433 were part of three multiwavelength campaigns, the first in conjunction with *ASCA* observations, the second simultaneous with a VLA-VLBA-MERLIN campaign, and the third associated with a Nobeyama millimeter-band campaign. All these campaigns included optical observations. Occurring at different jet precession and binary phases, the observations also monitored the system during a radio flare. The data provide SS 433's X-ray spectrum over more than an energy decade, and track the spectral variations as the X-ray source was partially eclipsed by its stellar companion. Detectable to ~ 50 keV, the continuum can be modeled as a power law with an exponential cutoff. Strong line emission is evident in the 5-10 keV range which can be modeled as a broad line whose energy is precession independent and a narrow line whose energy does vary with jet precession phase; this line model is clearly an oversimplification since *RXTE*'s PCA detector does not have sufficient energy resolution to detect the lines *ASCA* observed. Joint *ASCA-RXTE* fits are in progress. The eclipses are deeper at high energy and at jet precession phases when the jets are more inclined towards and away from us.

A large radio flare occurred between two sets of X-ray monitoring observations; an X-ray observation at the peak of the flare found a softer spectrum with a flux $\sim 1/3$ that of the quiescent level. I noted this bizarre relationship between the X-ray spectrum and radio flaring in the *Einstein* and *EXOSAT* observations.

RXTE Observations of SS 433: I. The X-ray Data

D. Band

X-2, MS B-220, Los Alamos National Laboratory, Los Alamos, NM 87545

P. Blanco, R. Rothschild,

CASS 0424, University of California at San Diego, La Jolla, CA 92093-0424

N. Kawai, T. Kotani, T. Oka

*Cosmic Radiation Laboratory, The Institute of Physical and Chemical Research (RIKEN), 2-1
Hirosawa, Wako, Saitama 351-01, Japan*

R. M. Wagner¹

Department of Astronomy, Ohio State University, 174 West 18th Avenue, Columbus, OH 43210

R. Hjellming, M. Rupen

NRAO, Socorro, NM 87801-0387

and

W. Brinkmann

MPI, Giessenbachstrasse, D-85740 Garching, Germany

ABSTRACT

We observed the jet-producing compact binary system SS 433 with *RXTE* during three multiwavelength campaigns, the first in conjunction with *ASCA* observations, the second simultaneous with a VLA-VLBA-MERLIN campaign, and the third associated with a Nobeyama millimeter-band campaign. All these campaigns included optical observations. Occurring at different jet precession and binary phases, the observations also monitored the system during a radio flare. The data provide SS 433’s X-ray spectrum over more than an energy decade, and track the spectral variations as the X-ray source was partially eclipsed. The continuum can be modeled as a power law with an exponential cutoff, which can be detected to ~ 50 keV. Strong line emission is evident in the 5–10 keV range which can be modeled as a broad line whose energy is precession independent and a narrow line whose energy does vary with jet precession phase; this line model is clearly an oversimplification since the PCA does not have sufficient energy resolution to detect the lines *ASCA* observed. The eclipses are deeper at high energy and at jet precession phases when the jets are more inclined towards and away from us. A large radio flare occurred between two sets of X-ray monitoring observations; an X-ray observation at the peak of the flare found a softer spectrum with a flux $\sim 1/3$ that of the quiescent level.

Subject headings: X-rays: binaries—X-rays: stars—stars: individual (SS 433)

1. Introduction

The Galactic compact binary system SS 433 is a unique laboratory of astrophysical phenomena: SS 433’s jets and accretion disk link it to morphologically similar systems such as young stars and active galaxies; the jet velocity of $0.26c$ may place SS 433 in the new class of Galactic “micro-quasars;” the 162.5 day jet precession is similar to the precession observed in systems such as Her X-1; and the P-Cygni profiles of some of the optical lines indicate that SS 433 has a high mass-loss wind. A comprehensive review of the system’s rich phenomenology can be found in Margon (1984). Our current conception of the system is a neutron star (D’Odorico et al. 1991) accreting gas from a companion through an accretion disk; the oppositely-directed jets with an opening angle of $\sim 5^\circ$ are accelerated perpendicular to the disk. The system is characterized by a 13.08 day binary period, and by the 162.5 day precession and 6.28 day nodding periods (Katz et al. 1982) of the jet (and presumably the disk).

The relativistic jets in SS 433 were revealed by Doppler-shifted optical line emission; this emission also constrains the physical conditions and excitation of the gas entrained in the jets (Begelman et al. 1980). The optical lines originate $\leq 10^{15}$ cm from the system, whereas the X-rays

¹Mailing address: Lowell Observatory, 1400 West Mars Hill Road, Flagstaff, AZ 86001

are emitted $\sim 10^{12}$ cm from the binary (as will be discussed below). The plasma in the jets must be accelerated close to the X-ray-emitting region, and therefore the X-rays are a diagnostic of freshly entrained plasma (e.g., Brinkmann et al. 1988, 1991). To probe the structure and physical conditions of the X-ray source we observed the system with *RXTE*, *ASCA*, radio, millimeter and optical telescopes. Here we present the *RXTE* observations.

Our goals were to answer the following questions:

1. What is the spectrum of SS 433 above 10 keV? *Ginga* observed SS 433 to 28 keV (Yuan et al. 1995); is there flux above this, and if so, is it from a different component?
2. How does this spectrum change when the X-ray source is partially eclipsed? During the eclipse the stellar companion blocks the radiation from different parts of the X-ray emitting region; thus from the spectra during the eclipse we can identify where various spectral components originate.

Based on the answers to these observational questions we can model the structure and physical conditions of the plasma within the jets near the site where it is accelerated. The result will be the run of temperature, density, filling factor, cooling rate, etc., near the base of the jets.

Ever since SS 433 was first detected as an X-ray source by *Ariel V* (Ricketts et al. 1981), SS 433 has been observed many times (*HEAO 1*—Marshall et al. 1979; *Ariel VI*—Ricketts et al. 1981; *Einstein*—Grindlay et al. 1984; *Tenma*—Matsuoka et al. 1986; *EXOSAT*—Watson et al. 1986; *Ginga*—Kawai et al. 1989; *ASCA*—Kotani et al. 1994; Kotani 1998). Most of these missions found the X-ray source to be variable; the spectrum has usually been described as a thermal Bremsstrahlung continuum, $T \geq 10$ keV, with a strong iron line (0.5 – 1 keV equivalent width). *Tenma* (Matsuoka et al. 1986) and *EXOSAT* (Watson et al. 1986) reported that the iron $K\alpha$ line complex had an energy shift consistent with an origin in the blue-shifted jet (i.e., in whichever jet had a velocity component towards the observer at the time of the observation); the apparent absence of a red-shifted line was interpreted to indicate that the X-ray emission originated within the inner 10^{12} cm of the jet which would be occulted by the accretion disk around the compact object. The iron line complex in the *Ginga* spectra were modeled by a stationary broad line and a narrow line whose energy was consistent with an origin in the “blue” jet (Brinkmann et al. 1991; Yuan et al. 1995). However, both red- and blue-shifted Fe, Si, S, Ca, Ar and Ni line emission identified in the recent *ASCA* spectra (with much higher spectral resolution than spectra from previous detectors—Kotani et al. 1994; Kotani 1998) show the X-ray emission must originate somewhat further out in the jets. The strength of the line emission indicates that a large fraction of the X-ray emission occurs within the jets. Therefore the X-rays probe the state of the plasma entrained by the jets very close to the compact object.

The *EXOSAT* (Stewart et al. 1987) and *Ginga* (Kawai et al. 1989; Brinkmann et al. 1991) observations of SS 433 over the binary period of 13.08 days show a decrease in intensity at the time of the primary optical eclipse which both demonstrates that the compact object is eclipsed during the primary eclipse, and locates a large fraction of the X-ray emission close to the compact object.

The depth of the eclipse depends on the precession angle, with a weak eclipse when the jets are in the plane of the sky ($\psi_{162} \sim 0$ using the standard ephemeris), and a deep eclipse when the jets are at their maximum inclination relative to the sky ($\psi_{162} \sim 0.65$). The extent of the deep eclipse varies with energy: at high energy ($E \geq 20$ keV) the eclipse is very deep ($\sim 80\%$) while at low energy ($E \leq 5$ keV) it is barely a ripple ($\sim 10\%$). The *Ginga* spectra were best-fitted by a Bremsstrahlung spectrum of $T \sim 30$ keV outside of the eclipse which softened to $T \sim 12$ keV during the eclipse (Yuan et al. 1995). This softening during the eclipse suggests that the temperature decreases with distance along the jet such that the companion star occults the higher temperature inner portion during the primary eclipse.

In this paper we present the *RXTE* data, while in subsequent papers we correlate these observations with related multiwavelength data. §2 presents the *RXTE* data, and §3 describes the fits to these data. The consequences of these observations are discussed in §4.

2. The X-Ray Data

We observed SS 433 with *RXTE* during three different campaigns. The first campaign monitored the source during a primary eclipse in 1996 April in conjunction with *ASCA* observations. The second campaign in 1998 March marked the beginning of a VLA-VLBA-MERLIN campaign, while the third set of observations in 1998 April coincided with a series of Nobeyama observations. Since SS 433 was flaring between the second and third campaigns, we also observed the source once between these campaigns.

RXTE includes three detector systems. The Proportional Counter (PCA) consists of 5 large Xe multiwire, multilayer, gas proportional counters covering 2–60 keV with an energy resolution of 1 keV at 6 keV (Jahoda et al. 1996). The large area of ~ 7000 cm² has advanced the sensitivity in this energy band to a qualitatively different level. The High Energy X-ray Timing Experiment (HEXTE) uses NaI(Tl)/CsI (Na) phoswich detectors to cover the 15–250 keV energy band with an energy resolution of 9 keV at 60 keV (Rothschild et al. 1998). HEXTE has two clusters of 4 detectors each; however, the spectroscopy electronics for one of the detectors died soon after launch. The total area of the 7 operational detectors is 1400 cm². HEXTE's background is measured by alternately chopping the two clusters on and off the source, and thus the average on-source area is only half the total area. Both the PCA and HEXTE provide no imaging data. The third *RXTE* instrument is the All Sky Monitor (ASM), three scanning shadow cameras utilizing position-sensitive Xe proportional counters which cover 1.5–12 keV with ~ 30 cm² each (Levine et al. 1996). The ASM can provide fluxes every 90 minute orbit, although fluxes for the brightest X-ray sources are calculated daily. SS 433 is at the ASM's detection threshold of ~ 10 mCrab, and the light curve consists predominantly of upper limits.

The *RXTE* data were broken up into a series of observations, each of which consisted of data from one or more spacecraft orbits. Each count during these observations is provided, and

therefore it is possible to break these observations into shorter accumulations. Similarly these observations can be summed into accumulations over longer periods. We extracted spectra for groups of observations which occurred close to each other in time. In some cases one or two of the 5 PCA detectors turned on or off during an observation (two of the detectors are more sensitive to the radiation environment than the other three). We only accumulated spectra while the same detector complement is on. As described below, we performed joint fits to spectra with different numbers of PCA detectors accumulated over nearby time ranges.

We extracted spectra for the PCA and the two HEXTE clusters separately, using the methodology for faint sources current in 1998 December. We included time segments more than 30 minutes after an SAA passage, when the magnetospheric electron flux was low (the “electron” parameter was less than 0.1), and when SS 433 was more than 10° above the horizon and was within 0.1° of the center of the detectors’ field-of-view. As mentioned above, we accumulated spectra over periods when the complement of PCA detectors which were on did not change. The PCA background was calculated using the model for faint sources current in December 1998, and the PCA response matrix was calculated with the energy-to-channel model “PCA.energy2chan.v3.0”. As is currently standard in PCA spectral analysis, we added a systematic error factor to the Poisson statistics uncertainty for each spectral channel.

HEXTE’s response is not thought to have changed over the course of the mission (except for the loss of one detector before the SS 433 observations), and therefore we use the same response matrices for each cluster for all the observations. On the other hand, the PCA response does change slowly, and therefore we calculated a response matrix for each campaign (i.e., we assume the changes in the detector response to be insignificant on the timescale of 1–2 weeks). We used the appropriate PCA response matrix for the detector complement which was on.

Table 1 lists the resulting 29 observations along with their date (in MJD–50000), binary and precession phases, and livetime. The observations are grouped into 3 campaigns (identified by prefixes ‘a’, ‘b’ and ‘d’) with one observation (with prefix ‘c’) between the second and third campaigns. The binary ephemeris we use is

$$\text{MJD } 46595.75 \pm 0.04 + n(13.0820 \pm 0.0007) \quad (1)$$

(Gladyshev et al. 1987) which places $\phi_{13.08} = 0$ at the primary eclipse. The precession ephemeris is

$$\text{MJD } 43561.87 \pm 0.04 + n(162.50) \quad (2)$$

(Margon & Anderson 1989) for which $\psi_{162} = 0$ occurs when the two jets are in the plane of the sky before the usually red-shifted jet becomes blue-shifted.

3. Spectral Fits

Before fitting all the observations systematically, we explored fitting different datasets with various models. We performed joint fits of the spectra from the PCA and the two HEXTE clusters;

however, we found that SS 433 is detected only to ~ 50 keV, and thus the HEXTE detectors effectively do not extend the spectral coverage of the PCA. Because of uncertainties in the detector calibrations, we included inter-detector normalizing constants as fitted parameters for any joint fits. These constants varied considerably from observation to observation, leading us to conclude that the HEXTE spectra do not add significance to our fits. We performed joint fits to all our observations with results consistent with the fits to the PCA spectra alone reported here. We fit the PCA and PCA+HEXTE spectra, excluding the 5–10 keV energy band, with a power law with exponential cutoff continuum model, which we found describes the continuum satisfactorily (see below). Figure 1 compares the values of E_p , the energy of the peak of $E^2 N_E \propto \nu f_\nu$, for the resulting fits. The differences between the E_p values for the two fits are less than the uncertainties, indicating not only that the values are consistent with each other, but that the PCA data dominates the fits to the PCA+HEXTE spectra.

Before discussing the fits in detail, we point out some general features. Even though SS 433 is a relatively weak source, the PCA’s effective area is so large that the uncertainties resulting from counting statistics are very small in the ~ 2.5 –25 keV band. On the other hand the spectral resolution is insufficient to resolve the multitude of lines which *ASCA* found (Kotani 1998). Thus the PCA spectra are very sensitive to a) systematic detector uncertainties and b) sub-resolution spectral features. Where *ASCA* spectra are available, such as during the 1996 April observations, a joint *RXTE-ASCA* fit will help detect the different lines.

The spectral model can be broken into the continuum and the spectral features in the 5–10 keV band. We will discuss each aspect separately. Since the PCA spectrum begins at 2.5 keV, the fits are relatively insensitive to N_H less than 10^{22} cm $^{-2}$. In exploratory fits we found that when we fitted the spectra with a power law+line model (which below we show is an inadequate model), the fitted values of N_H were large ($N_H \sim 2.5 \times 10^{22}$ cm $^{-2}$), but a cutoff power law+line fit gave much small values of N_H ; the absorption compensated for the inadequate continuum model. Consequently, we fixed the N_H at $N_H = 0.67 \times 10^{22}$ cm $^{-2}$, consistent with the values found by *ASCA* (Kotani 1998).

To determine the continuum without attempting to model the line complex at ~ 6.5 keV, we excluded the 5–10 keV channels from the continuum fits. The lines *ASCA* found between 2.5 and 5 keV had an order of magnitude less flux than those in the 5–10 keV band (Kotani 1998). The simplest continuum we tried was a power law. The resulting fits had a large reduced χ^2 , and systematic trends in the residuals. In particular, the model overpredicts the high energy spectrum. Therefore we added an exponential cutoff to the power law, resulting in an extremely significant reduction in χ^2 . The dashed curve in Figure 2a shows the cumulative distribution of $\Delta\chi^2$ resulting from the addition of a single parameter, the cutoff energy; the median value is 252.2 (this is the value of $\Delta\chi^2$ for a cumulative fraction of 1/2). The photon spectral index was frequently near $\alpha = 1.4$ ($N_E \propto E^{-\alpha}$), suggestive of a Bremsstrahlung continuum; the *Ginga* spectra were well-fit by a Bremsstrahlung spectrum (Yuan et al. 1995). Therefore we also tried a Bremsstrahlung continuum. The solid curve in Figure 2a is the cumulative distribution of $\Delta\chi^2$ comparing the

Bremsstrahlung and cutoff power law continua—a positive value indicates that the cutoff power law model had a smaller χ^2 . In this case the median value is 26.8. Note that technically the Bremsstrahlung model is not nested in the cutoff power law, i.e., the Bremsstrahlung model is not a cutoff power law with α fixed, and the calculation of the significance of the additional parameter in the cutoff power law model is not straightforward; nonetheless, the χ^2 improvement is clearly significant. In particular, there are some spectra which are radically different from a Bremsstrahlung spectrum. The cutoff power law model is statistically acceptable with a median $\chi^2 = 67.9$ for 77 degrees-of-freedom (vs. the Bremsstrahlung model's median $\chi^2 = 99.3$ for 78 degrees-of-freedom). Throughout the remainder of this analysis we use the cutoff power law model with parameters determined from fits excluding the 5–10 keV channels.

The iron line complex at ~ 6.5 keV is apparent to the eye in the count spectrum; fits to PCA spectra including the 5–10 keV channels without at least a single line result in extremely high χ^2 (e.g., $\chi^2=29757$ for 94 channels!). *ASCA* found a large number of lines in this complex which are clearly beyond the PCA's resolution. Joint fits to simultaneous *ASCA-RXTE* observations will be able to model this energy band; however for the majority of the *RXTE* observations this is not possible.

The line complex in the *Ginga* spectra was modeled by two lines, one narrow and the second broad. When the multiple line photon spectrum observed by *ASCA* was folded through the *Ginga* detector response, the resulting model count spectrum could be fitted satisfactorily by two lines (Yuan et al. 1995). Consequently, we decided to fit two lines to the 5–10 keV energy band; one line was forced to be narrow (its width was set to 0 in XSPEC), and the other was forced to have finite width. Since we know from the *ASCA* observations that this two line model is not accurate, and we do not want the inaccurate line model to affect the continuum, we froze the parameters of the cutoff power law model at their values from a fit to the spectrum excluding the 5–10 keV channels. The procedure was therefore to fit the PCA spectra except for the channels between 5 and 10 keV with the cutoff power law continuum (with N_H frozen at $6.7 \times 10^{21} \text{ cm}^{-2}$). Then we fitted the spectrum including the 5–10 keV channels, adding in two Gaussian lines (one with zero width, the other with nonzero width), but holding the continuum parameters fixed. Adding the two parameter narrow Gaussian line to a single broad line resulted in a median χ^2 improvement of 149.1; Figure 2b shows the distribution of $\Delta\chi^2$. The resulting fits are generally acceptable, with a median χ^2 of 73.1 for a spectrum with 94 channels. Fitting the continuum simultaneously with the two lines gives a median $\Delta\chi^2$ of only 8.2 and the $\Delta\chi^2$ distribution in Figure 2b. Our analysis below uses the fits with the continuum fixed when the two lines are fitted.

Figures 3a-c show the 2–10 keV (x's) and the 10–60 keV (diamonds) energy fluxes versus binary phase for each observation campaign (the observation between the second and third campaign is not included here, but is discussed below). Expected at $\phi_{13.08} = 0$, the primary eclipse is deep and convincing in both energy ranges for the first campaign, although there is insufficient data outside of the eclipse to establish an uneclipsed baseline. There is a convincing decrease at high energy but only a suggestive dip at low energies for the second and third campaigns; during these two

campaigns there are fluctuations after the eclipses which are comparable to the amplitude of the eclipses, at least at low energy. Unfortunately, the evidence for the eclipses in the second and third campaign relies on only one or two observations. As will be discussed below, the second campaign preceded and the third campaign straddled two radio flares, and thus the X-ray variability outside of the eclipses may be related to system flaring. Without previous X-ray observations (Steward et al. 1987; Kawai et al. 1989; and Brinkmann et al. 1991) and the expectation of an eclipse, the existence of an X-ray eclipse would probably not have been deduced from the *RXTE* observations alone.

The eclipses may be deeper at high energy than at low energy because the jet plasma cools as it moves away from the binary system, with high energy emission originating closer to the base of the jet. Thus the gas eclipsed by the stellar companion is at a higher temperature than for the uneclipsed gas. Similarly, the angle of the jets to the line-of-sight may explain why the eclipse is deeper during the first campaign than during the second and third campaigns. The projected angle between the central source and a given gas parcel in the jets decreases as the angle between the jets and the line-of-sight decreases, and therefore more of the jet is eclipsed when this angle is small. The second and third campaigns occurred when the precession phase was $\psi_{162} \sim 0$ and $\psi_{162} \sim 0.2$ when the jet directions are close to the plane of the sky and shallow eclipses are expected; on the other hand, $\psi_{162} \sim 0.8$ for the first campaign, near the jet’s maximum inclination out of the plane of the sky, when the eclipse should be deepest. Previous observations also reported both trends (Steward et al. 1987; Kawai et al. 1989; and Brinkmann et al. 1991). Using the low point at the bottom of the eclipse and the flux level outside of the eclipse, we estimate the depth of the eclipse (fraction of flux occulted) as 0.31 and 0.60 in the 2–10 and 10–60 keV bands, respectively, during the first observation, 0.09 and 0.37 during the second observation, and <0.07 and 0.42 during the third observation.

The power law continuum’s exponential cutoff also shows the eclipse. Figures 4a-c show E_{cut} (asterisks), the energy of the exponential cutoff, and a related energy $E_p = (2 - \alpha)E_{cut}$ (diamonds), the energy of the peak of $E^2 N(E) \propto \nu f_\nu$; E_p shows the photon energy where the emission occurs. The eclipse is particularly well-defined in the E_p lightcurve for the first campaign where the value drops by a factor of ~ 2 .

The continuum’s spectral index is surprisingly constant at $\alpha \sim 1.4$, which is why a Bremsstrahlung model is often an acceptable description of the continuum. There is no apparent correlation with the eclipse, although the spectrum does soften (α increases) during a radio flare (as discussed below).

In general, the broad spectral line has a centroid energy of ~ 6.85 keV which is fairly constant (Figures 5a-d). During the second and third campaigns the narrow line energy is ~ 6.4 keV. Surprisingly, the line energies appear to be correlated with the eclipse during the first campaign (Figure 5b): during the eclipse the narrow line energy decreased convincingly and the broad line energy increased less convincingly.

The narrow line energy is greater during the first campaign, when $\psi_{162} \sim 0.8$, than during the second and third campaigns, when $\psi_{162} \sim 0$ and ~ 0.2 . This shift in the narrow line is consistent qualitatively with the Doppler shift of lines emitted by the jet, with the jet inclined towards the observer dominating. However, the shift in the energy of the blueshifted lines between the first and second campaigns should be $\sim 10\%$, which is larger than observed. Figure 5a shows the expected red- and blueshifted energies for a line with a restframe energy of 5.575 keV, which is consistent with the narrow line energies during the second campaign; as can be seen, the narrow line energies of the first and third campaigns are not consistent with the prediction.

The flux of the broad line is approximately twice the flux of the narrow line. The broad line flux is also more variable than the narrow line flux, particularly during the first campaign (Figures 6a-d). However, when the equivalent width is considered rather than the absolute flux, the variability within a campaign is much smaller (Figures 7a-d). In particular, the eclipse is evident in the line flux but not in the equivalent width during the first campaign (Figure 6b vs. Figure 7b). The broad line flux is greater, and the narrow line flux smaller, during the first campaign compared to the second and third campaigns; this dependence of the broad line flux on jet precession phase was observed by *Ginga* (Yuan et al. 1995). The line flux and equivalent width of the observation between the second and third campaigns is significantly lower; this observation will be discussed below.

The source was not eclipsed during the observations at the end of both the second and third campaigns and consequently we added these observations to form two spectra each with $\sim 6.25 \times 10^4$ s livetime in the PCA. The source is detected up to ~ 35 keV in the PCA spectrum for the second campaign, and up to ~ 50 keV in the third one. Note that Figures 3–7 show that the source was variable over the period of these summed spectra. The resulting fit parameters are provided by Table 2, and the fits are shown by Figure 8.

As mentioned above, there was one observation between the second and third campaigns. The Green Bank Interferometer observations,² shown by Figure 9, detected a major radio flare which peaked at the time of these *RXTE* low points. The third *RXTE* and the Nobeyama campaigns occurred during the tail of this flare; a second flare occurred a few days after the end of this campaign. Unfortunately, this flaring was not well sampled by the *RXTE* observations. Not only did the X-ray flux drop by a factor of ~ 3 , but the spectrum also softened. Figure 10 shows that during the flare the spectral index increased, and indeed, at the peak of the flare the continuum is a power law $\sim E^{-2}$.

²The Green Bank Interferometer is a facility of the National Science Foundation operated by the NRAO in support of NASA High Energy Astrophysics programs.

4. Discussion

4.1. Correlation with Nobeyama Observations

The third set of *RXTE* observations coincided with a monitoring campaign with the Nobeyama Millimeter Array which consisted of 7 daily observations from MJD=50900 to 50907, skipping an observation at MJD=50905 (Kotani et al. 1999). During the first three observations the 89.7 and 101.7 GHz fluxes increased from 65 mJy to a peak at 150 mJy at MJD=50902, and then fell back to a flux of ~ 80 mJy. A somewhat similar pattern is seen in the X-ray fluxes (see Figure 3c). The Nobeyama observations begin in the middle of the primary eclipse and the millimeter flux peaks just after egress from the eclipse. As discussed above, there are radio flares 10 days before and after the Nobeyama and *RXTE* observations. As Figure 10 shows, the X-ray spectral index is softer at the beginning of the *RXTE* observations which coincide with the Nobeyama campaign; this figure indicates that the X-ray spectrum softens during the radio flare. Therefore, it is difficult to determine whether the millimeter flux variations are correlated with the binary period or with the source’s flaring.

4.2. Correlation with Radio Flaring

We have only one *RXTE* observation during the major radio flare between the second and third campaigns. At the peak of the radio flare the X-ray flux was only 1/3 the flux before and afterwards (Figure 9), and the spectrum was significantly softer (the photon spectral index is 2 rather than 1.4—Figure 10). This paradoxical behavior—a decrease in the X-ray flux when the source flares in the radio—has been noted before for SS 433, and appears to be typical of Galactic “microquasar” sources.

Band (1989) noted that SS 433’s X-ray behavior differed between radio flaring and quiescent phases. The average 1–10 keV flux observed by *Einstein* when there were radio flares (MJD 4147.6–4168.5, called “Einstein-1” by Band 1989) was half the flux during *Einstein* (MJD 4520.2–4521.4, called “Einstein-2” by Band 1989), *Tenma* (Matsuoka et al. 1986) and *EXOSAT* (Watson et al. 1986) observations when there were no radio flares. The X-ray variability was much greater during the flaring Einstein-1 epoch: factor of 2 variations on timescales of a day.

The *RXTE* spectrum softens during the radio flare. Similar behavior was observed during the *Einstein* observations. Note that the characterization of the *Einstein* spectra is based on fits of a power law (without any emission lines) to only 6 MPC channels covering 1–10 keV (Grindlay et al. 1984). In terms of the photon spectral index used here, $\alpha \sim 1.3$ during the non-flaring Einstein-2 epoch and the first of the Einstein-1 observations which might have been before the flaring began. During most of the Einstein-1 observations α is greater (the spectrum is softer), with softer spectra when the flux is smaller. For example, during the last flare, α decreased from 1.7 to 0.8 as the 1–10 keV flux increased from 7.2×10^{-11} to 2.3×10^{-10} erg cm $^{-2}$ s $^{-1}$. The *Einstein* spectra suggest

that the spectrum is soft before an X-ray flare, and hardens as the flare peaks.

Band (1989) notes a number of other phenomena which may be correlated with SS 433 flaring and quiescent phases. Crampton & Hutchings (1981) noted an increase in the scatter of the velocities of the stationary $H\beta$ line, and differences in the optical variability. They also found differences in the absorption lines during these two phases. Dopita & Cherepashchuk (1981) found a major change in the P Cygni lines during an optical outburst which preceded a radio flare. Based on the X-ray behavior and these optical phenomena, Band (1989) suggested that outflow associated with a flare may obscure part of the X-ray source; at least part of this outflow must be thermal gas which is at most only partially ionized (otherwise the X-rays will not be absorbed).

Similar behavior is seen in some “microquasars.” Mirabel et al. (1998) find that X-ray dips precede the appearance of hour-long infrared and radio flares with amplitudes of ~ 50 mJy in GRS 1915+105. However, during these dips the X-ray spectrum hardens, which is contrary to the observations of SS 433. An interpretation of the GRS 1915+105 phenomenon is that the inner part of the accretion disk is partially ejected, partially advected rapidly into the black hole, resulting in the diminution of the softer X-ray flux; the infrared and radio flares are synchrotron emission by the adiabatically expanding ejected material. Harmon et al. (1997) found an anticorrelation between the 20–100 keV and the radio fluxes on a timescale of a few days when GRS 1915+105 had both radio flares and jet ejection, although the opposite correlation is seen at other times. Note that there is a small ‘flare’ at the end of the second *RXTE* campaign (see Figures 3b and 9) 12 days before the radio flare.

5. Summary

RXTE made three sets of observations of SS 433 which coincided with *ASCA*, VLA-VLBA-MERLIN and Nobeyama campaigns, respectively. Each campaign covered a primary binary eclipse, when the stellar companion occults the compact object and the inner portion of the jets. The first campaign occurred when the jets were inclined out of the plane of the sky, while the jets were nearly in the plane of the sky during the second and third campaigns. As has been seen previously, the X-ray eclipse is deeper at high energies than at low energies, which can be explained by the occultation of hotter gas in the inner portion of the jets. Similarly, the eclipse is shallower when the jets are in the plane of the sky, which can be explained by the projected angle on the sky of a region of a given temperature in the jets.

The continuum can be described by a power law with an exponential cutoff; the photon number spectral index is fairly constant at 1.4 (i.e., $N_E \propto E^{-1.4}$) while the cutoff energy varies. Although the *RXTE* data extends to much higher energy than that of previous missions, there is no evidence of an additional X-ray component, or a deviation from the continuum determined by *Ginga*. The *RXTE* spectra lack sufficient spectral resolution to distinguish between all the lines revealed by the *ASCA* observations. Consequently, we fit the continuum over the spectrum without the 5–10 keV

channels, and then fit two spectral lines—one narrow and one broad—over the spectrum with the 5–10 keV channels holding the continuum parameters fixed.

A major radio flare occurred between the second and third set of observations. Fortunately, *RXTE* observed SS 433 at the peak of this flare. The X-ray flux is $\sim 1/3$ the flux during the observations before and after the flare. The continuum is a steeper power law $N \propto E^{-2}$ and the exponential cutoff is poorly constrained during the flare. Similar X-ray behavior was observed in *Einstein* observations of SS 433, and is seen during radio flares in the recently discovered “micro-quasars.”

This work was supported by NASA grants NAG5-3306, NAG5-7277 and NAG5-7643.

REFERENCES

- Band, D. 1989, *ApJ*, 336, 937
- Band, D. L., & Grindlay, J. E. 1984, *ApJ*, 285, 702
- Begelman, M. C., et al. 1980, *ApJ*, 238, 722
- Brinkmann, W., Kawai, N., & Matsuoka, M., 1989, *A&A*, 218, L13
- Brinkmann, W., Kawai, N., Matsuoka, M., & Fink, H. H. 1991, *A&A*, 241, 112
- Crampton, D., & Hutchings, J. B. 1981, *ApJ*, 251, 604
- D’Odorico, S., et al. 1991, *Nature*, 353, 329
- Dopita, M. A., & Cherepashchuk, A. M. 1981, *Vistas in Astronomy*, 25, 51
- Gladyshev, S. A., Goranskii, V. P., & Cherepashchuk, A. M. 1987, *Soviet Astron.*, 31, 541
- Grindlay, J. E., Band, D., Seward, F., Leahy, D., Weisskopf, M. C., & Marshall, F. E. 1984, *ApJ*, 277, 286
- Jahoda, K., et al. 1996, *EUV, X-ray and Gamma-Ray Instrumentation for Astronomy VII*, SPIE Proceedings, ed. O. H. V. Sigmund and M. Gummin, 2808, 59
- Katz, J. I., et al. 1982, *ApJ*, 260, 780
- Kawai, N. 1989, *Proc. 23rd ESLAB Symp.*, Bologna, p. 453
- Kawai, N., Matsuoka, M., Pan, H. C., & Stewart, G. C. 1989, *PASJ*, 41, 491
- Kotani, T. 1998, Ph.D. thesis, University of Tokyo

- Kotani, T., et al. 1994, PASJ, 46, L147
- 1999, in preparation
- Levine, A. M., et al. 1996, ApJ, 469, L33
- Margon, B. 1984, ARA&A, 22, 507
- Margon, B., & Andersen, S. 1989, ApJ, 347, 448
- Marshall, F. E., Swank, J. H., Boldt, E. A., Holt, S. S., & Serlemitsos, P. J. 1979, ApJ, 230, L145
- Matsuoka, M., Takano, S., & Makishima, K. 1986, MNRAS, 222, 605
- Mirabel, I. F., Dhawan, V., Chaty, S., Rodríguez, L. F., Martí, J., Robinson, C. R., Swank, J., & Geballe, T. R. 1998, A&A, 330, L9
- Pounds, K. A., et al. 1990, Nature, 344, 132
- Ricketts, M. J., Hall, R., Page, C. G., Pounds, K. A., & Sims, M. R. 1981, Vistas in Astronomy, 25, 71
- Rothschild, R. E., et al. 1998, ApJ, 496, 538
- Seaquist, E. R., Gilmore, W. S., Johnston, K. J., & Grindlay, J. E. 1982, ApJ, 260, 220
- Seward, F., Grindlay, J., Seaquist, E., & Gilmore, W. 1980, Nature, 287, 806
- Soong, Y., et al. 1990, ApJ, 348, 641
- Stewart, G. C. et al. 1987, MNRAS, 228, 293
- Watson, M. G., Willingale, R., Grindlay, J. E., & Seward, F. D. 1983, ApJ, 273, 688
- Watson, M. G., Stewart, G. C., Brinkmann, W., & King, A. R. 1986, MNRAS, 222, 261
- Yamauchi, S., Kawai, N., & Aoki, T. 1994, PASJ, 46, L109
- Yuan, W., Kawai, N., Brinkmann, W., and Matsuoka, M. 1995, A&A, 297, 451

Fig. 1.— Comparison of E_p for fits to PCA and PCA+HEXTE spectra. The spectra were fit with a power law with exponential cutoff continuum. The energy range 5–10 keV was excluded so that a model for the line features would not be necessary. Showing the photon energy where the bulk of the energy flux is emitted, E_p is the energy of the peak of $E^2 N_E \propto \nu f_\nu$. The HEXTE data for two observations were corrupted, and for one observation $\alpha > 2$ ($N_E \propto E^{-\alpha}$), resulting in $E_p < 0$. The uncertainties result from a propagation of errors assuming the parameters are uncorrelated.

Fig. 2.— The cumulative distribution of $\Delta\chi^2$ comparing continuum (panel a) and line (panel b) models. Panel a compares fits to PCA spectra from 2.5 to 60 keV, excluding the 5–10 keV band (where line emission is expected). For all models $N_H = 0.67 \times 10^{22} \text{ cm}^{-2}$. The solid curve compares a Bremsstrahlung model to an exponentially cutoff power law model; the Bremsstrahlung model is very nearly a cutoff power law with the photon spectral index fixed at $\alpha \sim 1.4$. The dashed curve compares a power law to the cutoff power law model. In both cases the single additional parameter is significant for the median value of $\Delta\chi^2$. The dashed curve in panel b presents the $\Delta\chi^2$ for the addition of a narrow line to a model with a cutoff power law continuum and a single broad Gaussian line. In these fits the continuum parameters are fixed at their values from a fit to the PCA spectrum excluding the 5–10 keV band; of course, the lines are fit to the spectrum including this band. The solid curve compares the fits with the continuum either fixed or fit simultaneously with the lines.

Fig. 3.— 2–10 keV (asterisks) and 10–60 keV (diamonds) energy fluxes as a function of the binary phase $\phi_{13.08}$ for the first (panel a), second (panel b) and third (panel c) campaigns. The phases of the primary eclipse are indicated.

Fig. 4.— E_{cut} (asterisks) and E_p (diamonds) as a function of the binary phase $\phi_{13.08}$ for the first (panel a), second (panel b) and third (panel c) campaigns. E_{cut} is the exponential cutoff energy and E_p is the energy of the peak of $E^2 N(E) \propto \nu f_\nu$.

Fig. 5.— Centroid energies of the broad (asterisks) and narrow lines (diamonds) fit to the PCA spectra as a function of the jet precession phase ψ_{162} for the entire dataset (panel a) and binary phase $\phi_{13.08}$ for the first (panel b), second (panel c) and third (panel d) campaigns. The two line model is an approximation to the multiline spectrum observed by *ASCA*. Also shown in panel a is the expected observed line energies for lines emitted at a rest frame energy of 5.575 keV in the two jets.

Fig. 6.— Broad (asterisks) and narrow (diamonds) line fluxes as a function of the jet precession phase ψ_{162} for the entire dataset (panel a) and binary phase $\phi_{13.08}$ (panels b-d) for the three different campaigns. The arrow at the bottom of panel a indicates the order in which the data were accumulated. The phases of the eclipse are shown on panels b-d.

Fig. 7.— The same as the previous figure for the line equivalent widths.

Fig. 8.— Fitted PCA spectra and residuals. Panel a shows the spectrum summed over observations b6–b12 (see Table 2), while panel b shows the spectrum summed over observations d6–d10 with all 5 PCUs on. The data have been rebinned to 3σ per displayed bin up to a maximum of 25 of the original bins (fits were performed on the unbinned data).

Fig. 9.— The 2.25 GHz (upper solid curve) and the 8.3 GHz (lower solid curve) fluxes from the Green Bank Interferometer during the 1998 X-ray observations (left hand axis). Superimposed are the X-ray fluxes (dashed curve, right hand axis). Diamonds indicate the X-ray observations when the source was not eclipsed.

Fig. 10.— The X-ray photon spectral index α ($N_E \propto E^{-\alpha}$) during the 1998 X-ray observations.

Table 1. Log of *RXTE* Observations

| Obs. ^a | MJD-50000 ^b | PCA Livetime ^c | $\phi_{13.08}$ ^d | ψ_{162} ^e |
|-------------------|------------------------|---------------------------|-----------------------------|---------------------------|
| a1 | 191.104–191.252 | 7456 | 0.8360–0.8473 | 0.7953–0.7962 |
| a2 | 192.105–192.251 | 6848 | 0.9125–0.9237 | 0.8014–0.8023 |
| a3 | 192.713–192.812 | 4960 | 0.9590–0.9666 | 0.8052–0.8058 |
| a4 | 193.062–193.385 | 5808 | 0.9856–0.0103 | 0.8073–0.8093 |
| a5 | 193.772–193.879 | 5952 | 0.0399–0.0480 | 0.8117–0.8124 |
| a6 | 194.914–195.119 | 9792 ^f | 0.1272–0.1429 | 0.8187–0.8200 |
| b1 | 868.778–868.954 | 8896 | 0.6380–0.6514 | 0.9656–0.9667 |
| b2 | 870.248–870.441 | 6064 ^f | 0.7504–0.7651 | 0.9746–0.9758 |
| b3 | 871.918–872.097 | 8720 | 0.8780–0.8917 | 0.9849–0.9860 |
| b4 | 873.182–873.348 | 9356 | 0.9746–0.9873 | 0.9927–0.9937 |
| b5 | 874.921–875.098 | 7968 | 0.1076–0.1211 | 0.0034–0.0045 |
| b6 | 876.728–876.815 | 2592 | 0.2457–0.2523 | 0.0146–0.0150 |
| b7 | 877.582–877.744 | 5776 | 0.3110–0.3233 | 0.0198–0.0208 |
| b8 | 877.793–878.000 | 9664 | 0.3271–0.3429 | 0.0211–0.0223 |
| b9 | 878.000–878.333 | 16288 | 0.3430–0.3683 | 0.0223–0.0244 |
| b10 | 878.582–878.958 | 15120 | 0.3874–0.4161 | 0.0259–0.0282 |
| b11 | 878.972–879.179 | 9712 | 0.4173–0.4331 | 0.0283–0.0296 |
| b12 | 879.251–879.709 | 8576 | 0.4385–0.4735 | 0.0300–0.0329 |
| c1 | 889.739–889.984 | 10176 ^f | 0.2403–0.2590 | 0.0946–0.0961 |
| d1 | 897.856–897.950 | 5024 | 0.8607–0.8679 | 0.1445–0.1451 |
| d2 | 898.789–898.977 | 8720 | 0.9321–0.9464 | 0.1503–0.1514 |
| d3 | 899.723–899.951 | 10592 | 0.0034–0.0209 | 0.1560–0.1574 |
| d4 | 900.728–901.017 | 12080 | 0.0803–0.1024 | 0.1622–0.1640 |
| d5 | 901.523–901.985 | 14304 ^f | 0.1411–0.1764 | 0.1671–0.1699 |
| d6 | 902.749–903.089 | 11872 | 0.2348–0.2608 | 0.1746–0.1767 |
| d7 | 903.729–904.029 | 11924 ^f | 0.3097–0.3326 | 0.1807–0.1825 |
| d8 | 904.724–905.231 | 23712 ^f | 0.3858–0.4245 | 0.1868–0.1899 |
| d9 | 905.666–906.164 | 17792 | 0.4577–0.4958 | 0.1926–0.1957 |
| d10 | 906.791–907.162 | 12000 ^f | 0.5437–0.5721 | 0.1995–0.2018 |

^aObservation name.^bModified Julian Day-50000.^cLivetime of the PCA observation.^dBinary orbital phase using $T_0 = 46595.75$ (MJD) and $P = 13.0820$ days.^ePrecession phase using $T_0 = 43561.87$ (MJD) and $P = 162.50$ days^fJoint fit between observations with different numbers of PCUs on.

Table 2. Fit Parameters for Two Summed Spectra

| Parameter ^a | Second Campaign | Third Campaign | Units |
|--|----------------------------------|----------------------------------|---|
| PCA livetime | 6.24×10^4 | 6.27×10^4 | s |
| N_H (fixed) | 6.7×10^{21} | 6.7×10^{21} | cm^{-2} |
| Continuum fit, excluding 5–10 keV channels | | | |
| n_c^b | $(3.96 \pm 0.06) \times 10^{-2}$ | $(4.16 \pm 0.06) \times 10^{-2}$ | $\text{ph keV}^{-1} \text{ cm}^{-2} \text{ s}^{-1}$ |
| α^c | 1.487 ± 0.017 | 1.557 ± 0.016 | |
| E_{cut}^d | 19.11 ± 0.80 | 21.87 ± 1.025 | keV |
| χ^2^e | 82.4 | 93.1 | |
| Bins | 80 | 80 | |
| Fitted parameters | 3 | 3 | |
| Broad and narrow line fit, holding continuum fixed | | | |
| n_{line}^f | $(2.16 \pm 0.07) \times 10^{-3}$ | $(1.99 \pm 0.07) \times 10^{-3}$ | $\text{ph cm}^{-2} \text{ s}^{-1}$ |
| E_{line}^g | 6.790 ± 0.018 | 6.799 ± 0.020 | keV |
| E_w^h | 0.837 ± 0.013 | 0.809 ± 0.014 | keV |
| n_{line}^i | $(8.90 \pm 0.06) \times 10^{-4}$ | $(8.54 \pm 0.64) \times 10^{-4}$ | $\text{ph cm}^{-2} \text{ s}^{-1}$ |
| E_{line}^j | 6.450 ± 0.017 | 6.392 ± 0.017 | keV |
| χ^2^k | 72.5 | 72.0 | |
| Bins | 94 | 94 | |
| Fitted parameters ^l | 5 | 5 | |

^aThe continuum model is a power law with an exponential cutoff which was fit to the PCA spectra excluding the 5–10 keV energy band. The two line model was fit to the spectra including the 5–10 keV channels, holding the continuum model fixed.

^bNormalization of the cutoff power law continuum.

^cPhoton spectral index.

^dEnergy of the continuum's exponential cutoff.

^e χ^2 of the continuum fit, with the 5–10 keV channels excluded.

^fFlux of the broad Gaussian line.

^gCentroid of the broad Gaussian line.

^hWidth of the broad Gaussian line.

ⁱFlux of the narrow Gaussian line.

^jCentroid of the narrow Gaussian line.

^k χ^2 of fitting the two lines to the entire spectrum holding the continuum fixed at the above parameters.

^lNumber of parameters in the two line model.

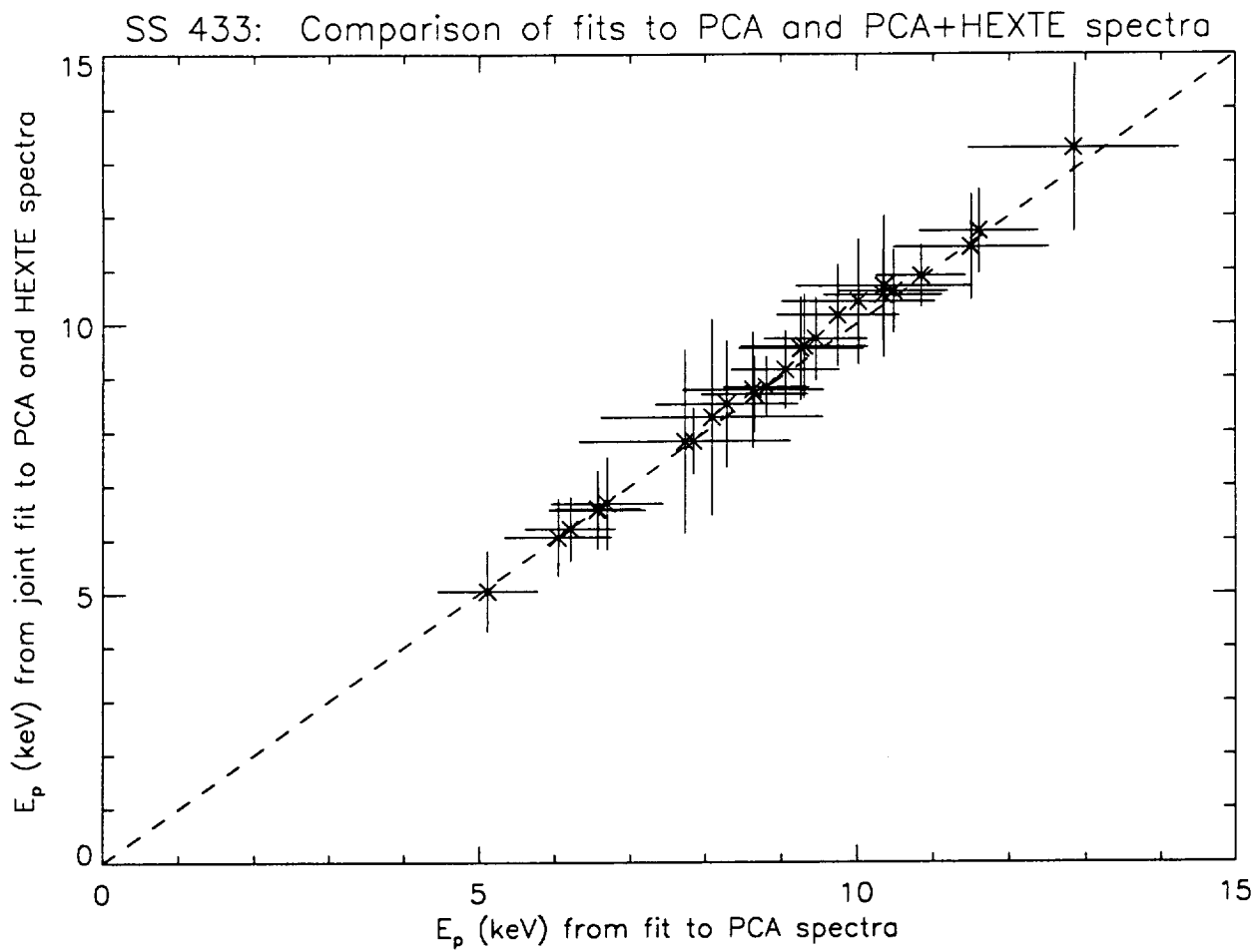


Fig. 1

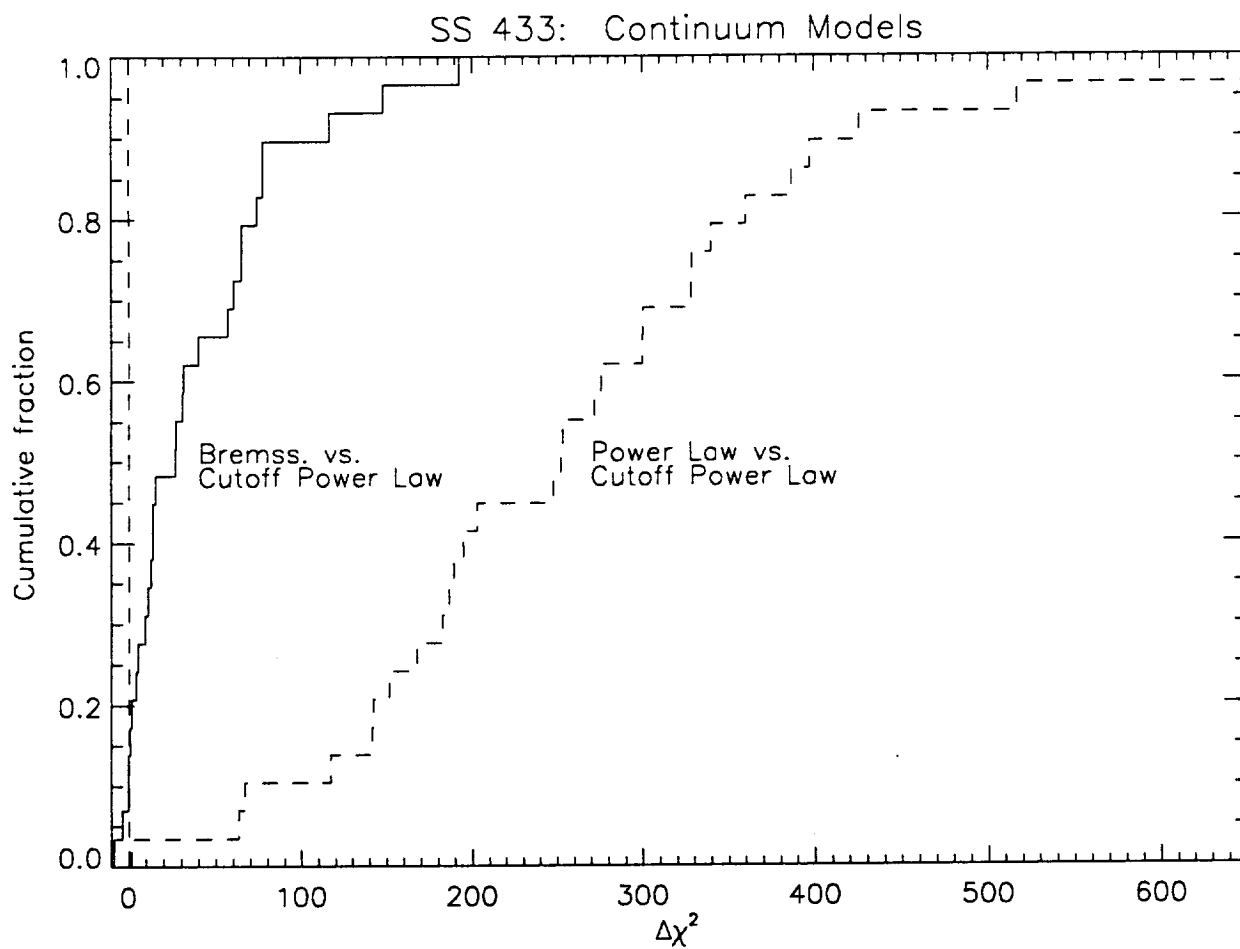


Fig 2a

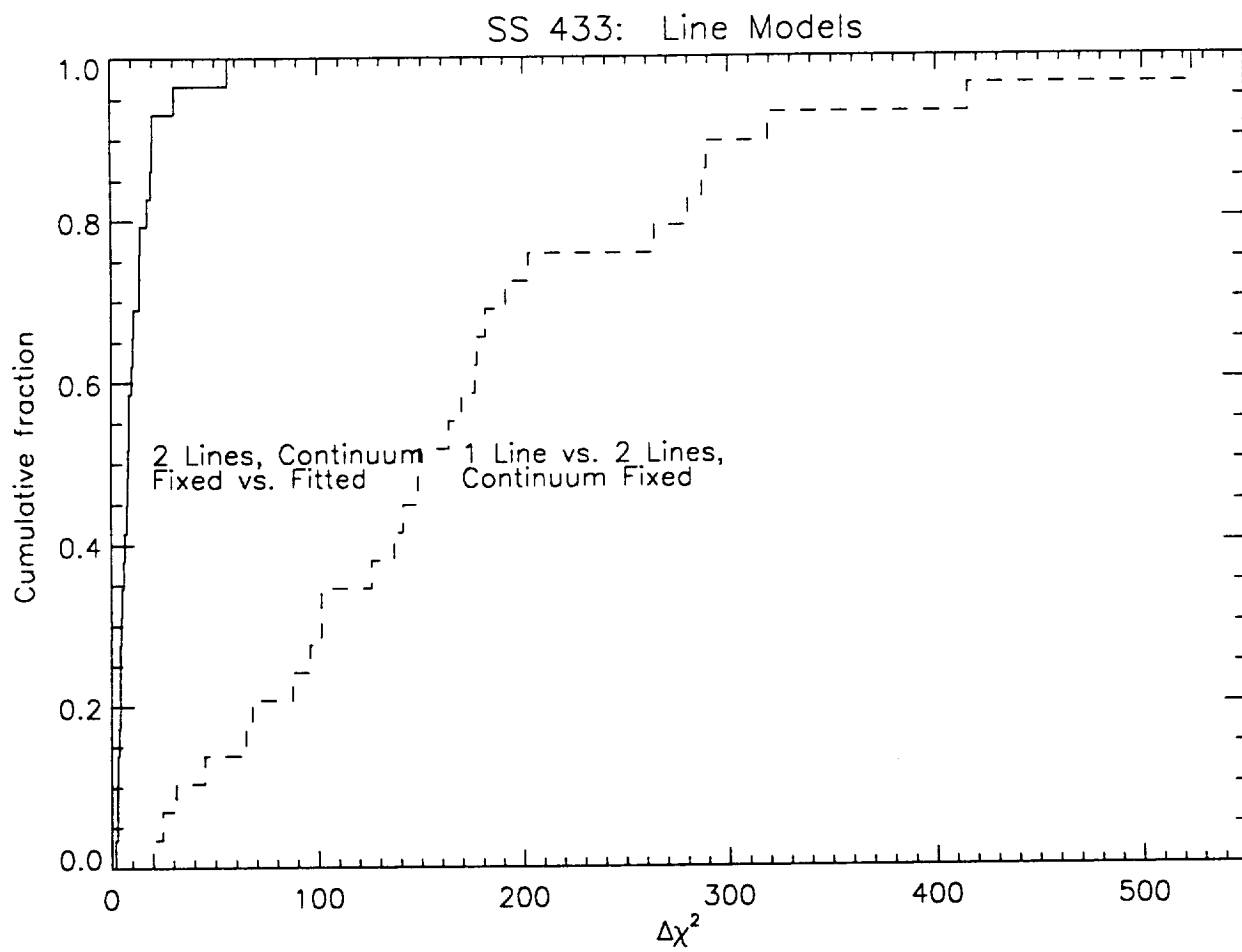


Fig. 2b

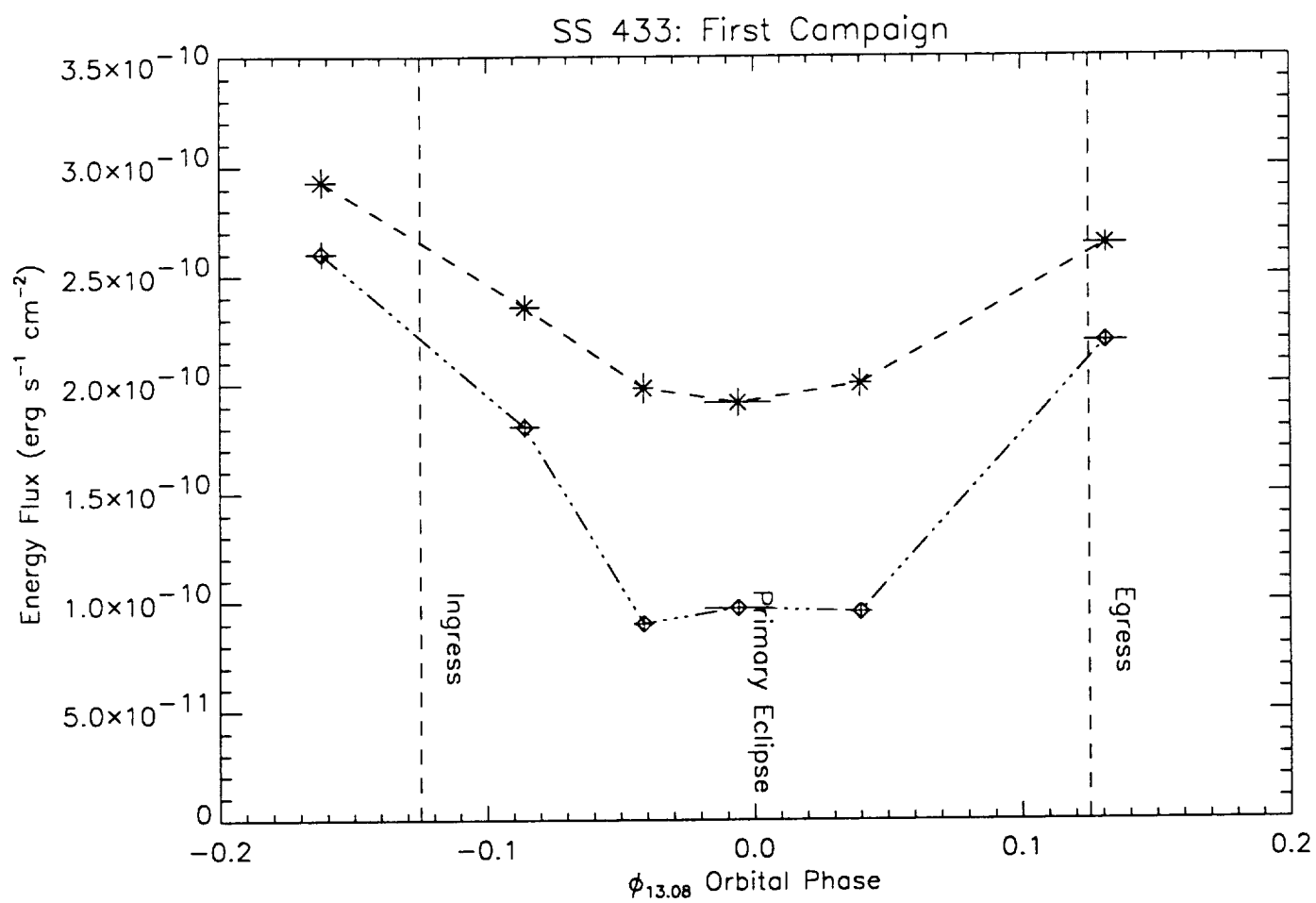


Fig 3a

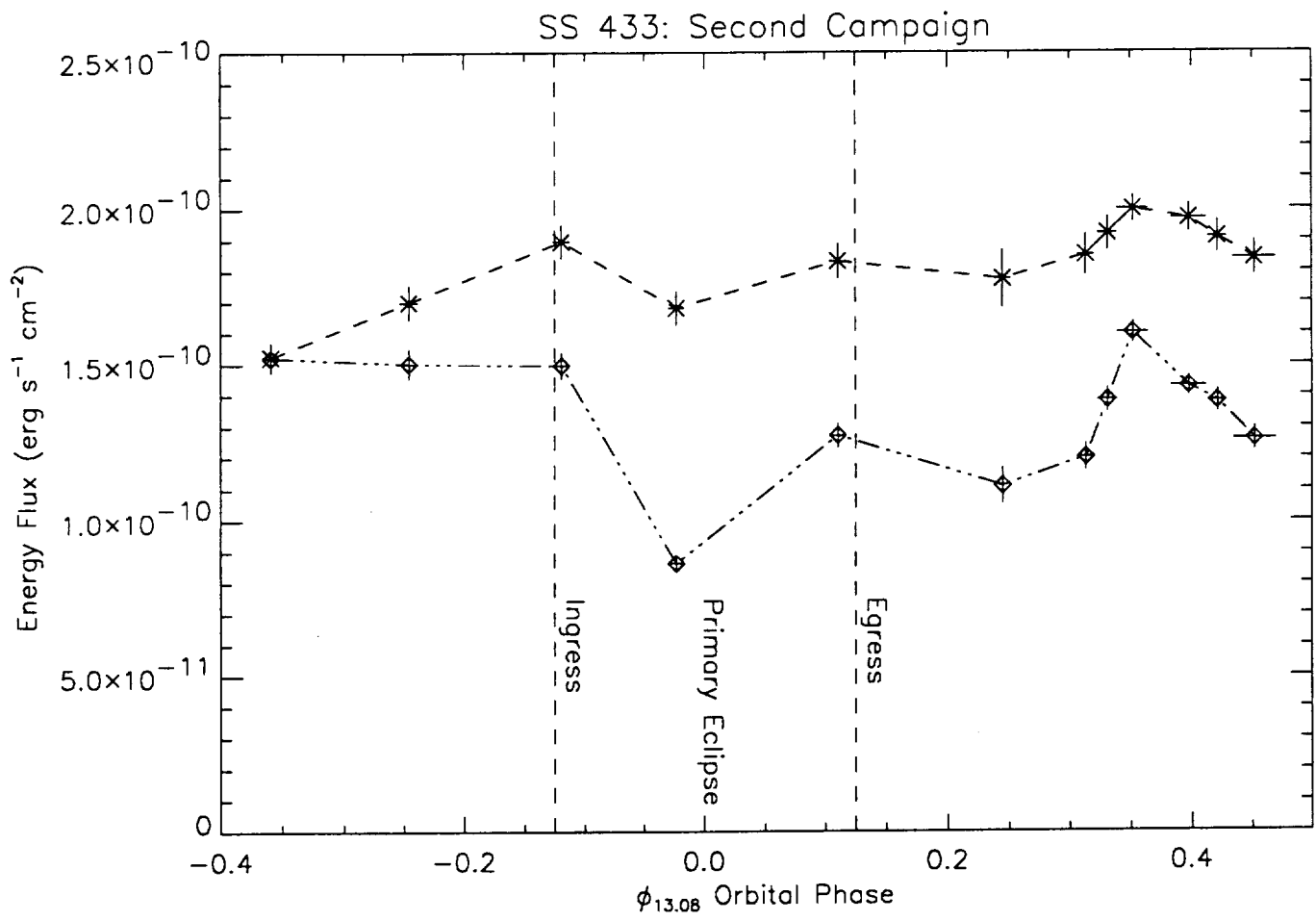


Fig 36

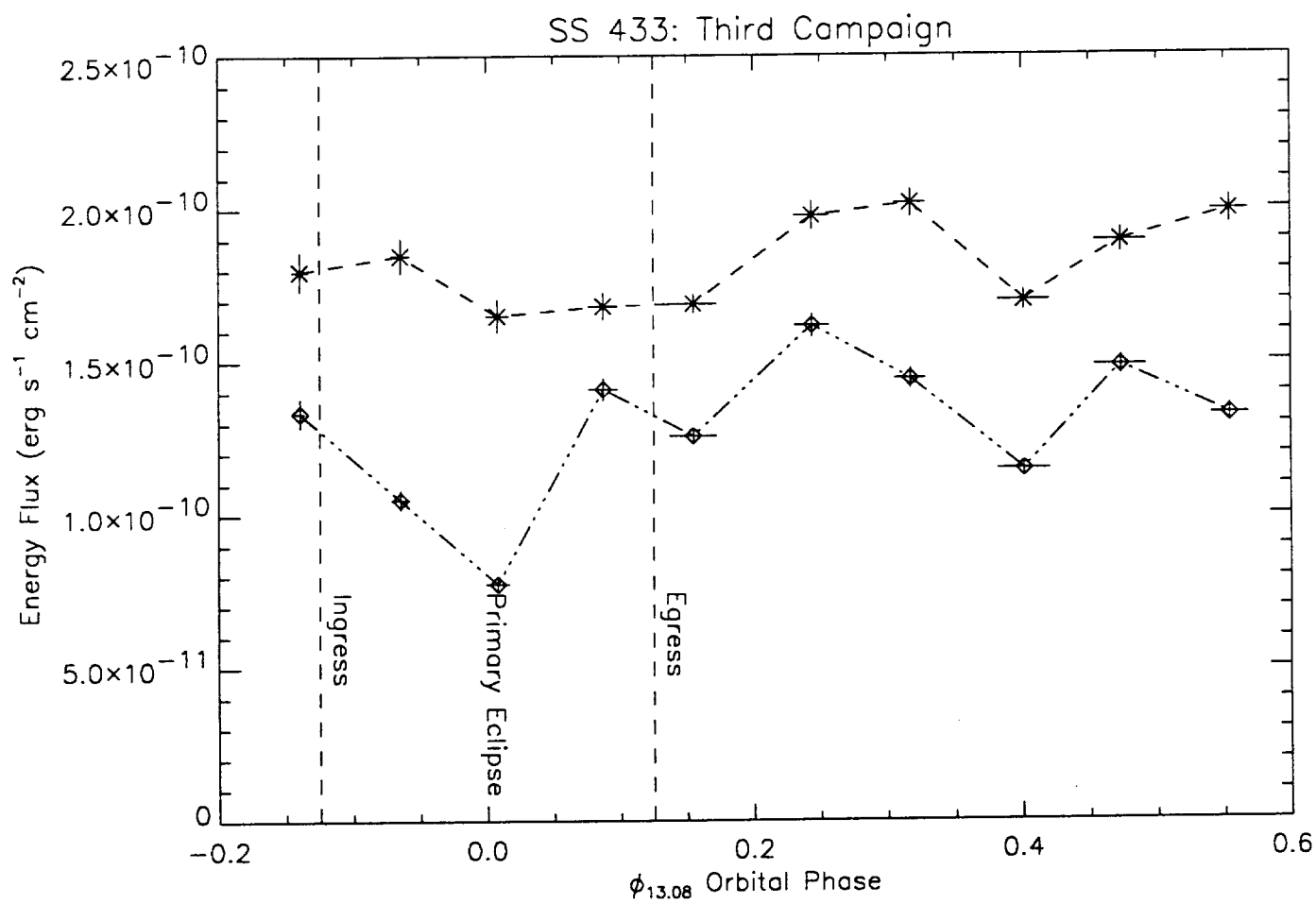


Fig 3c

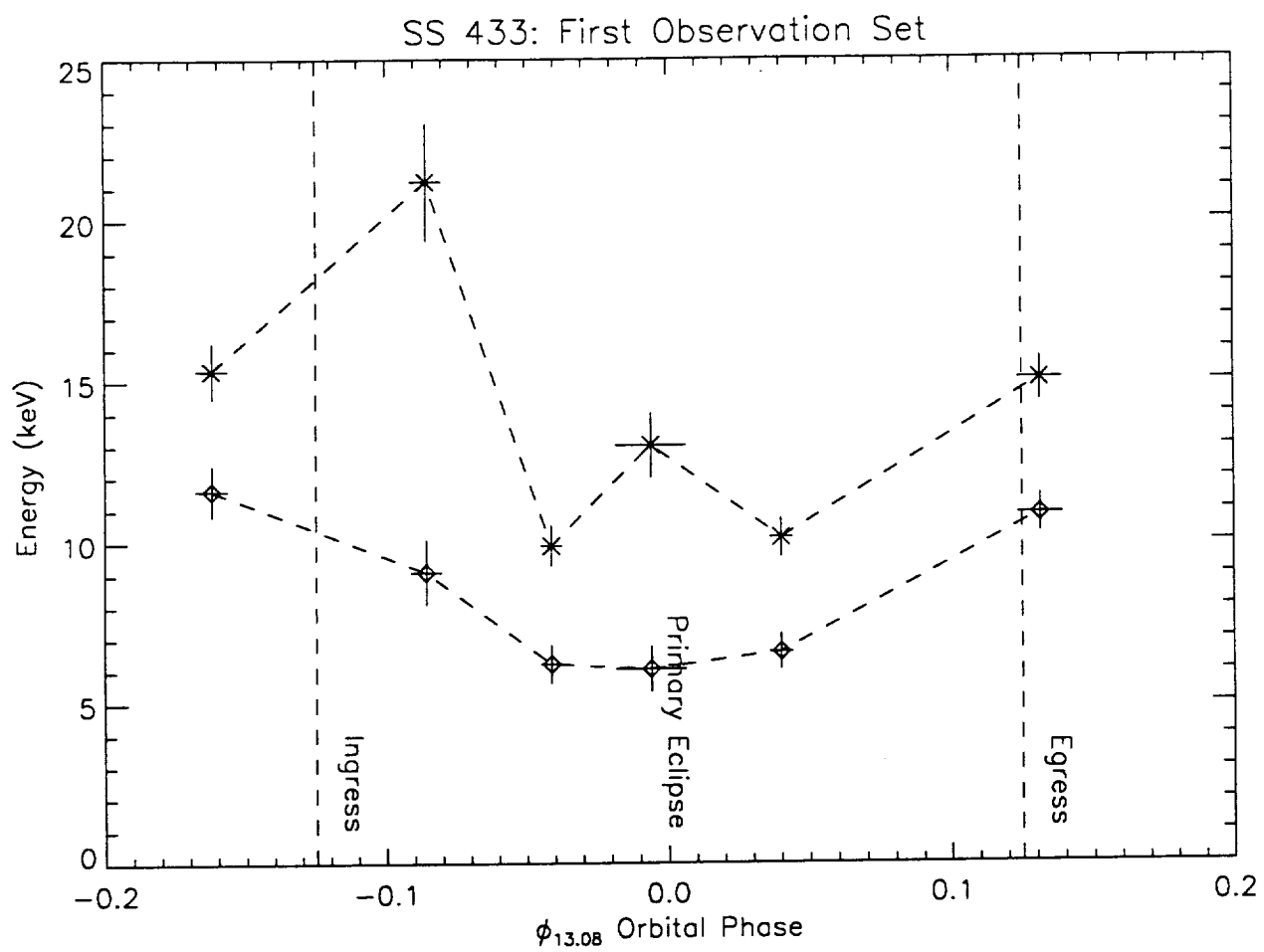


Fig. 4a

SS 433: Second Observation Set

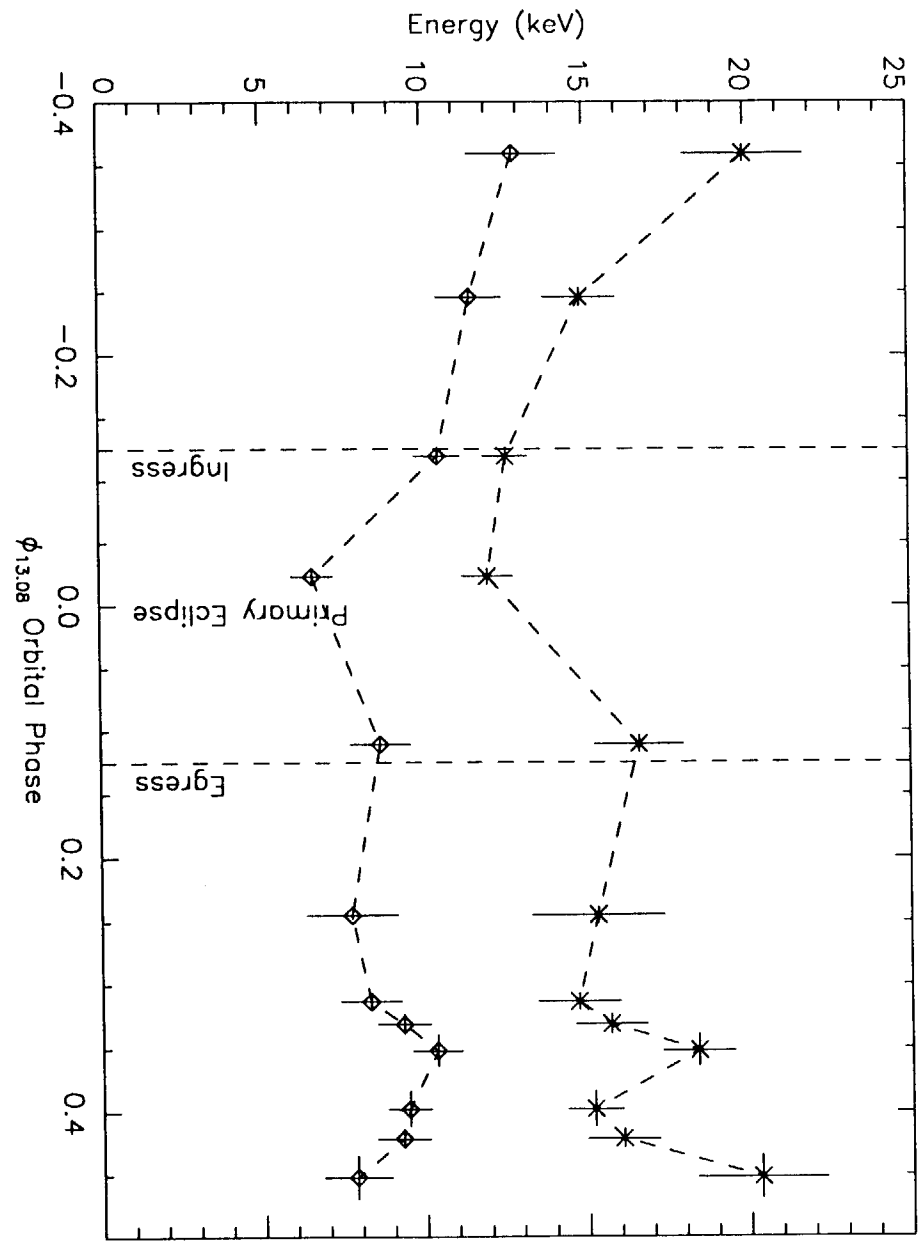


Fig. 4b

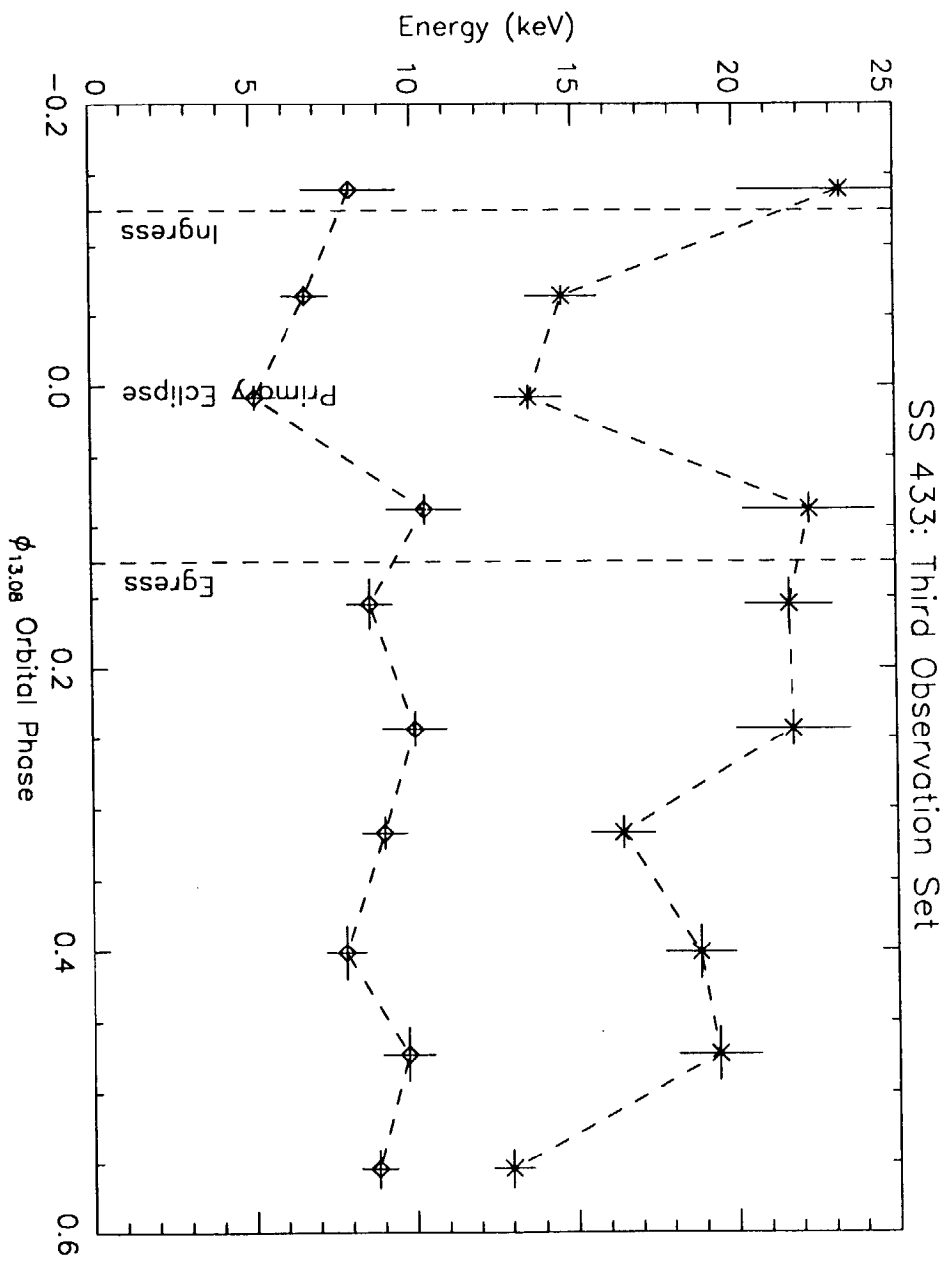


Fig. 4c

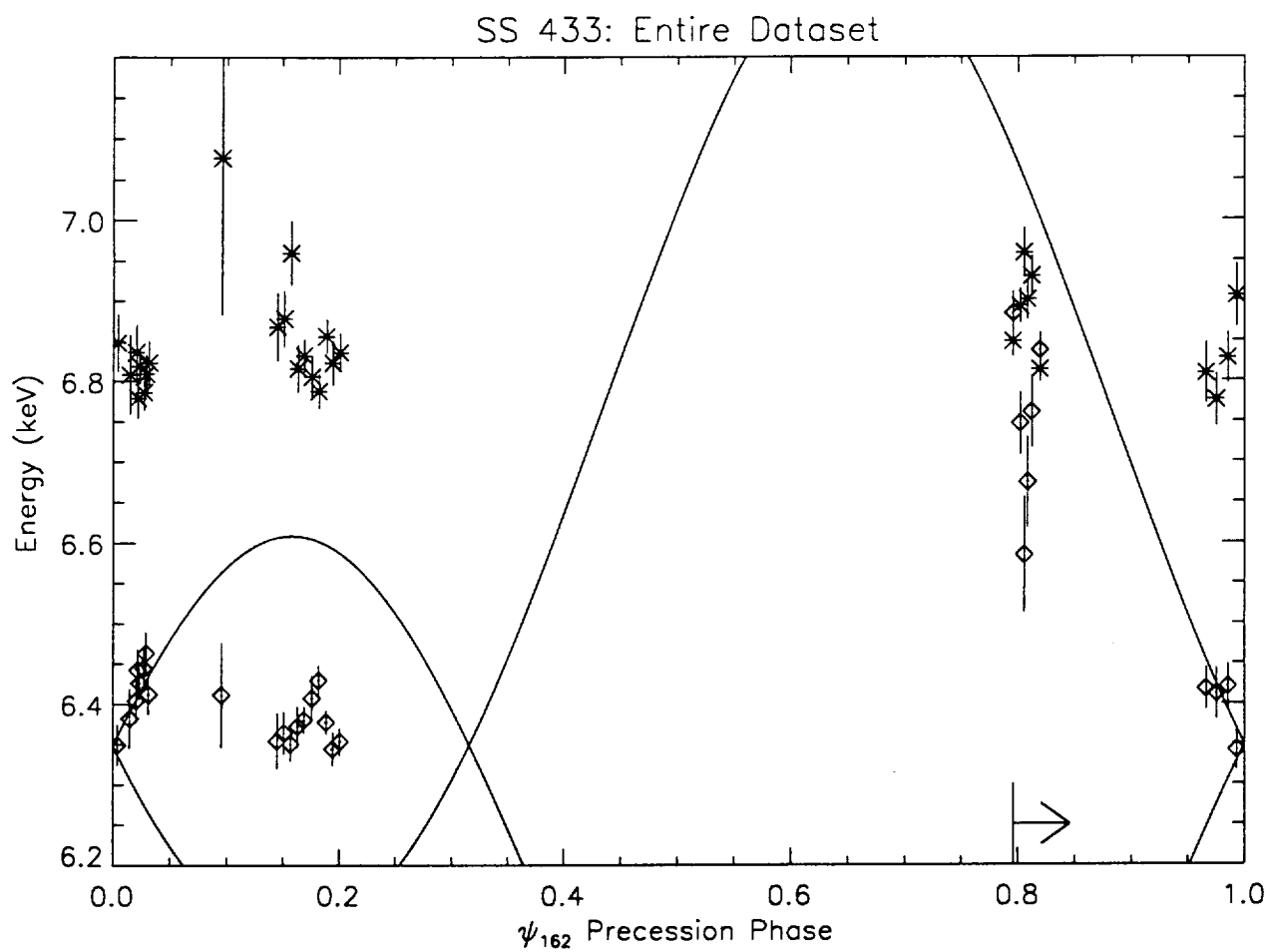


Fig. 5a

SS 433: First Campaign

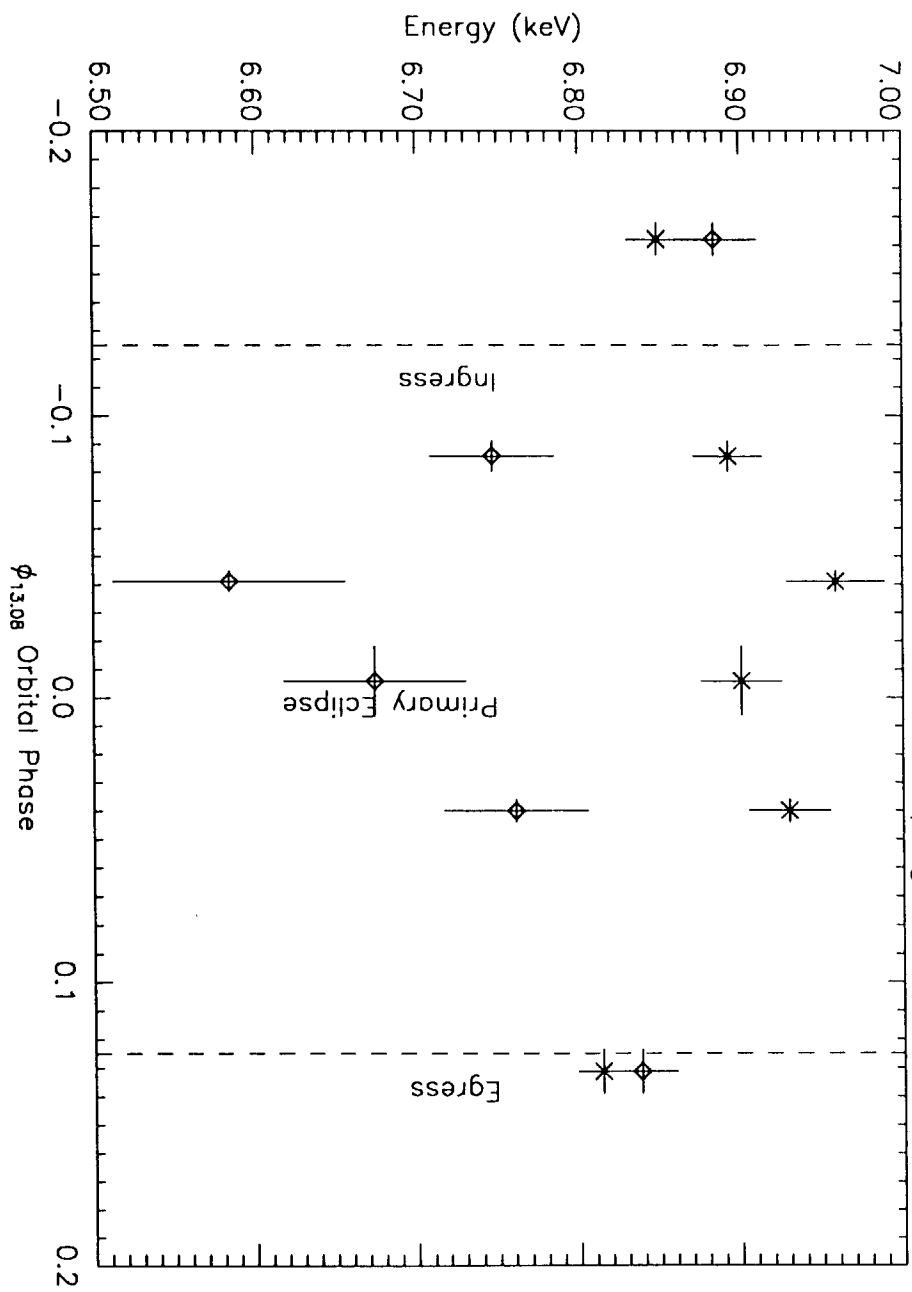


Fig 56

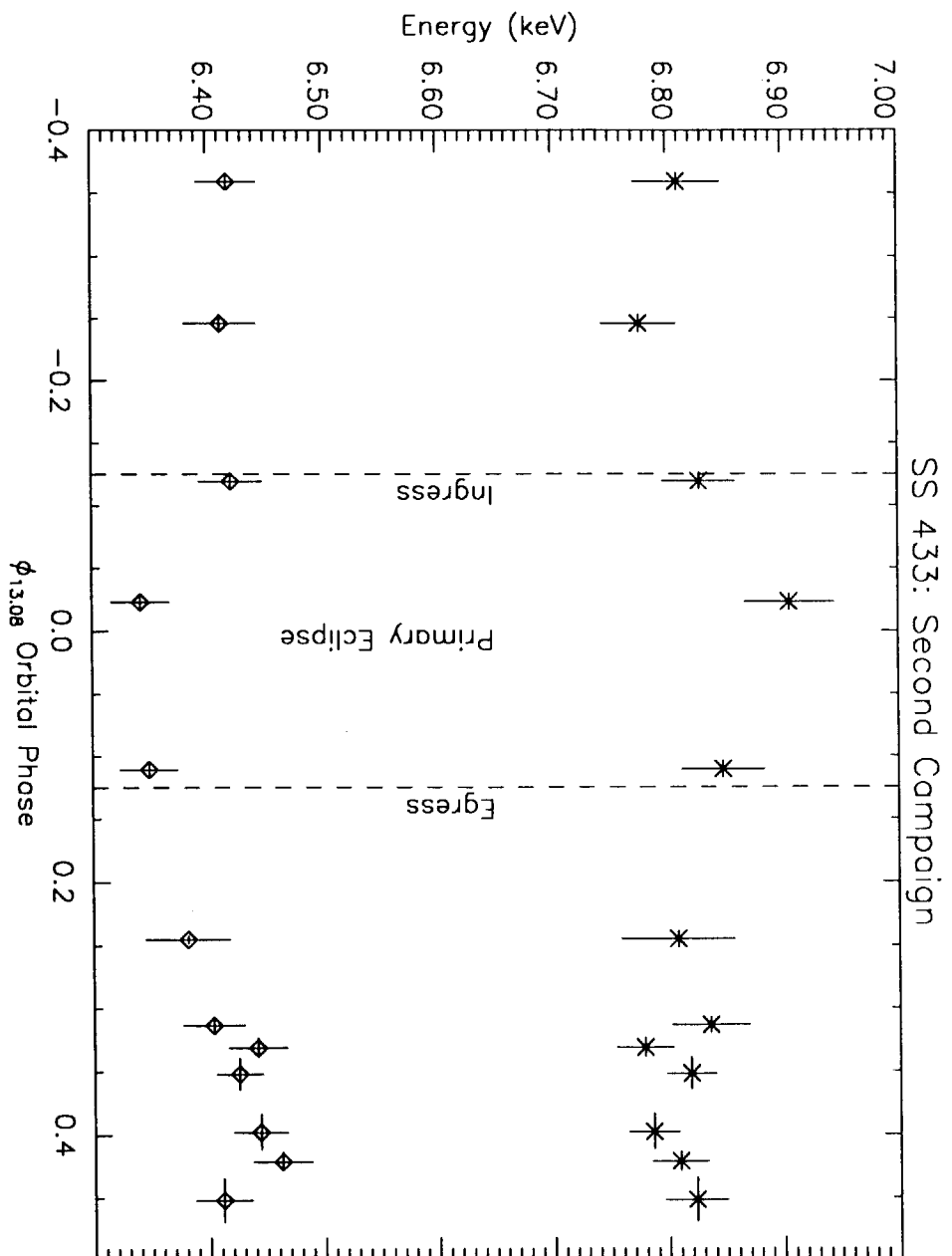


Fig. 5c

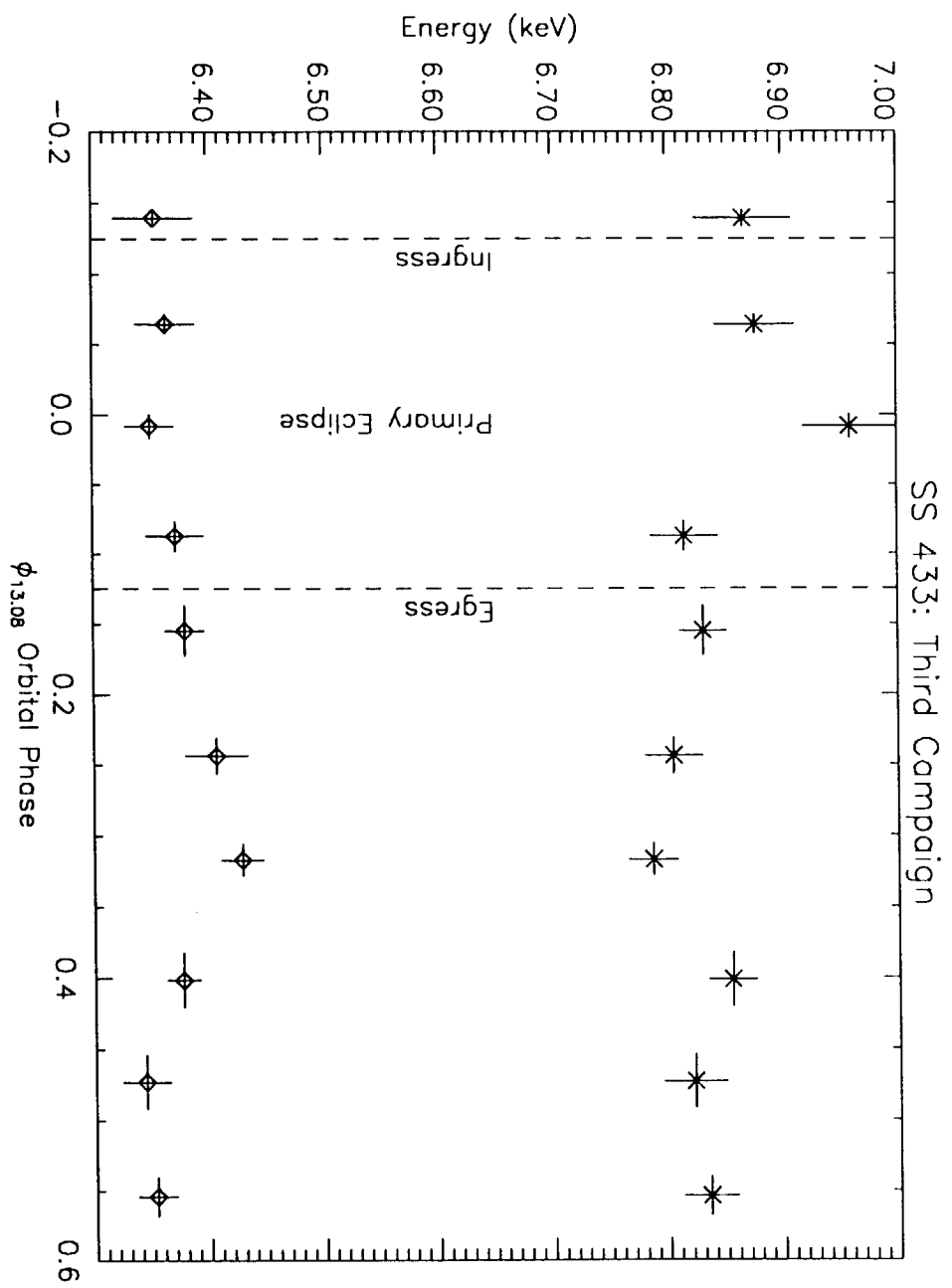


Fig. 5d

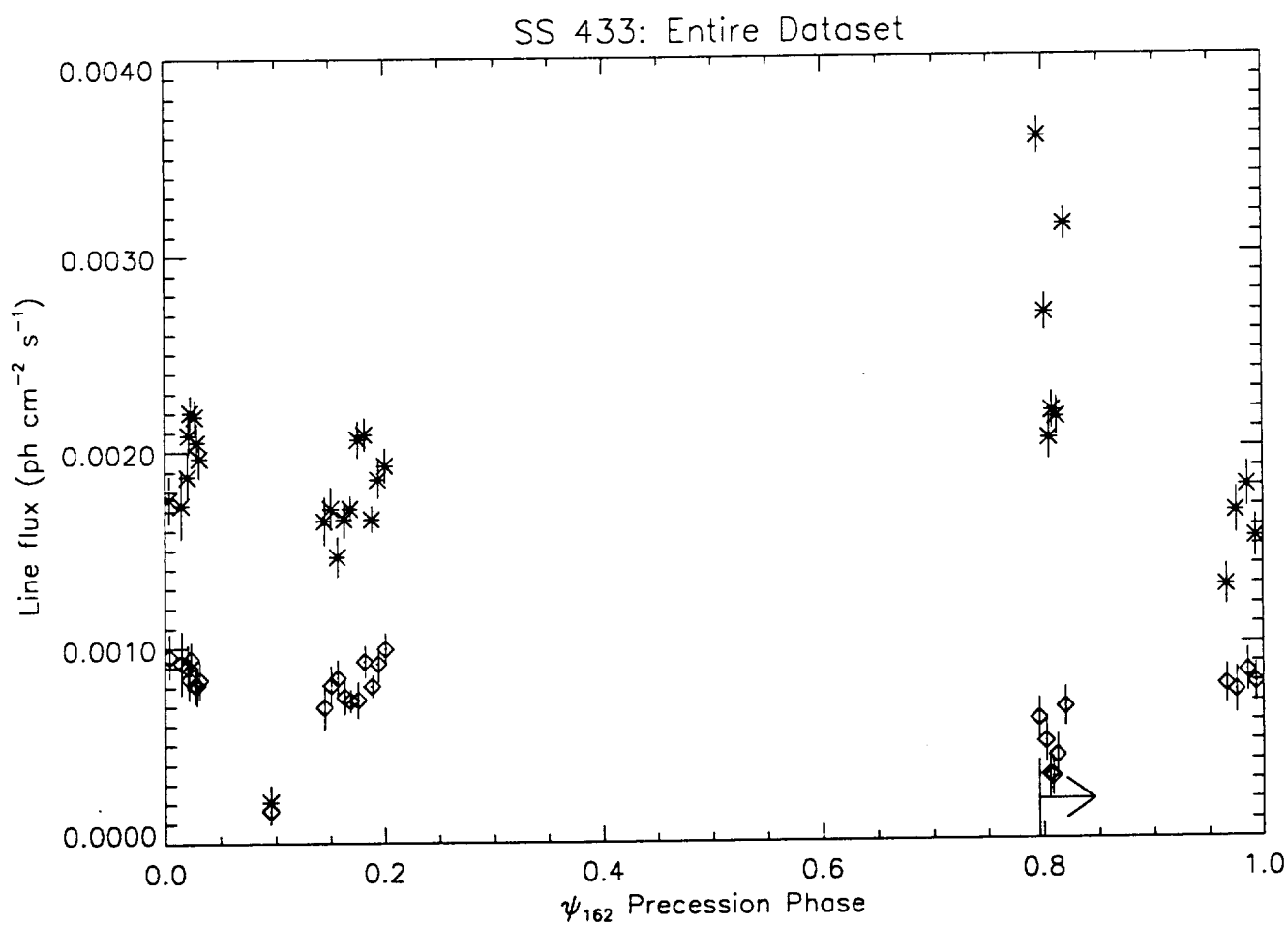


Fig 6a

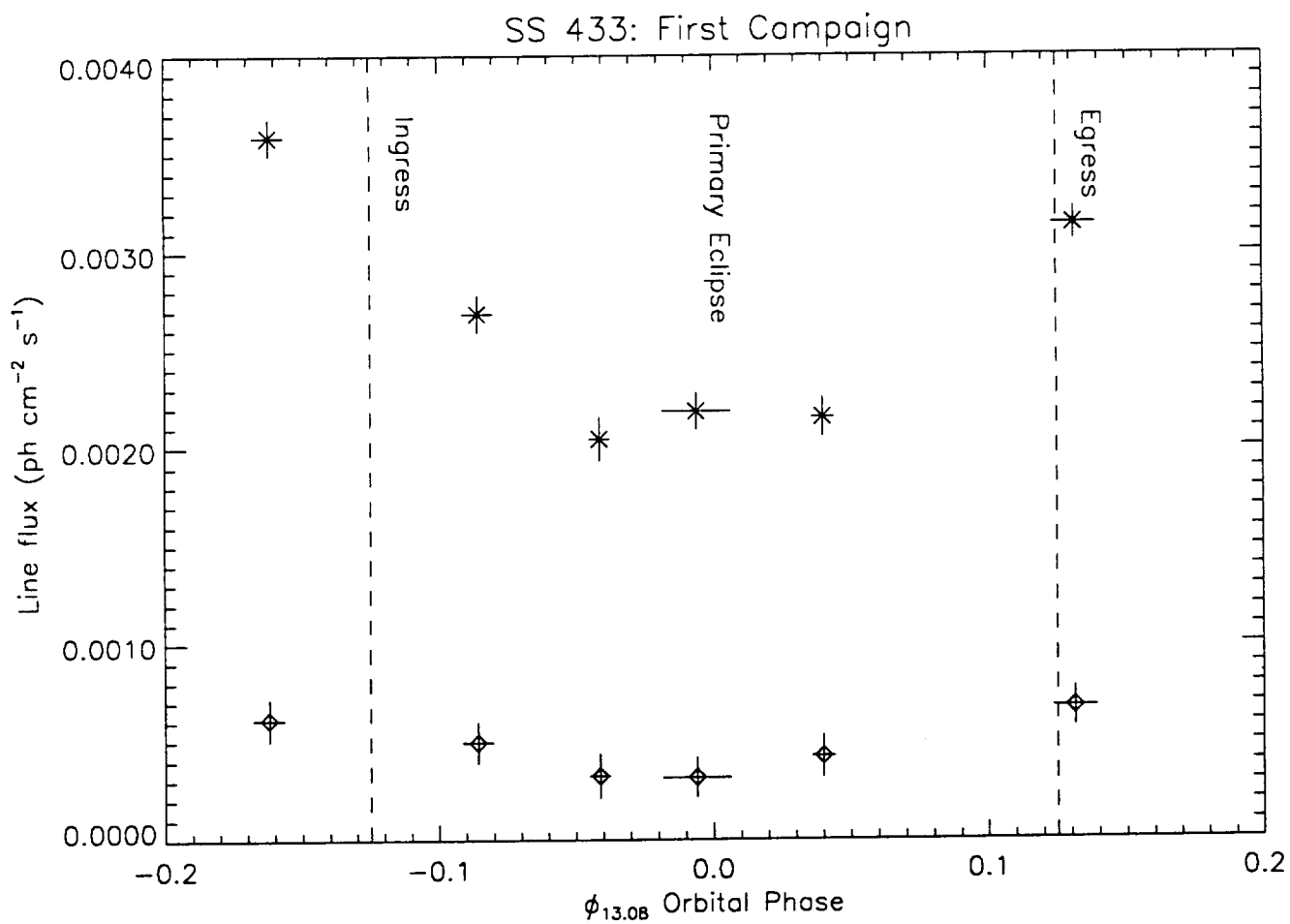


Fig 6t

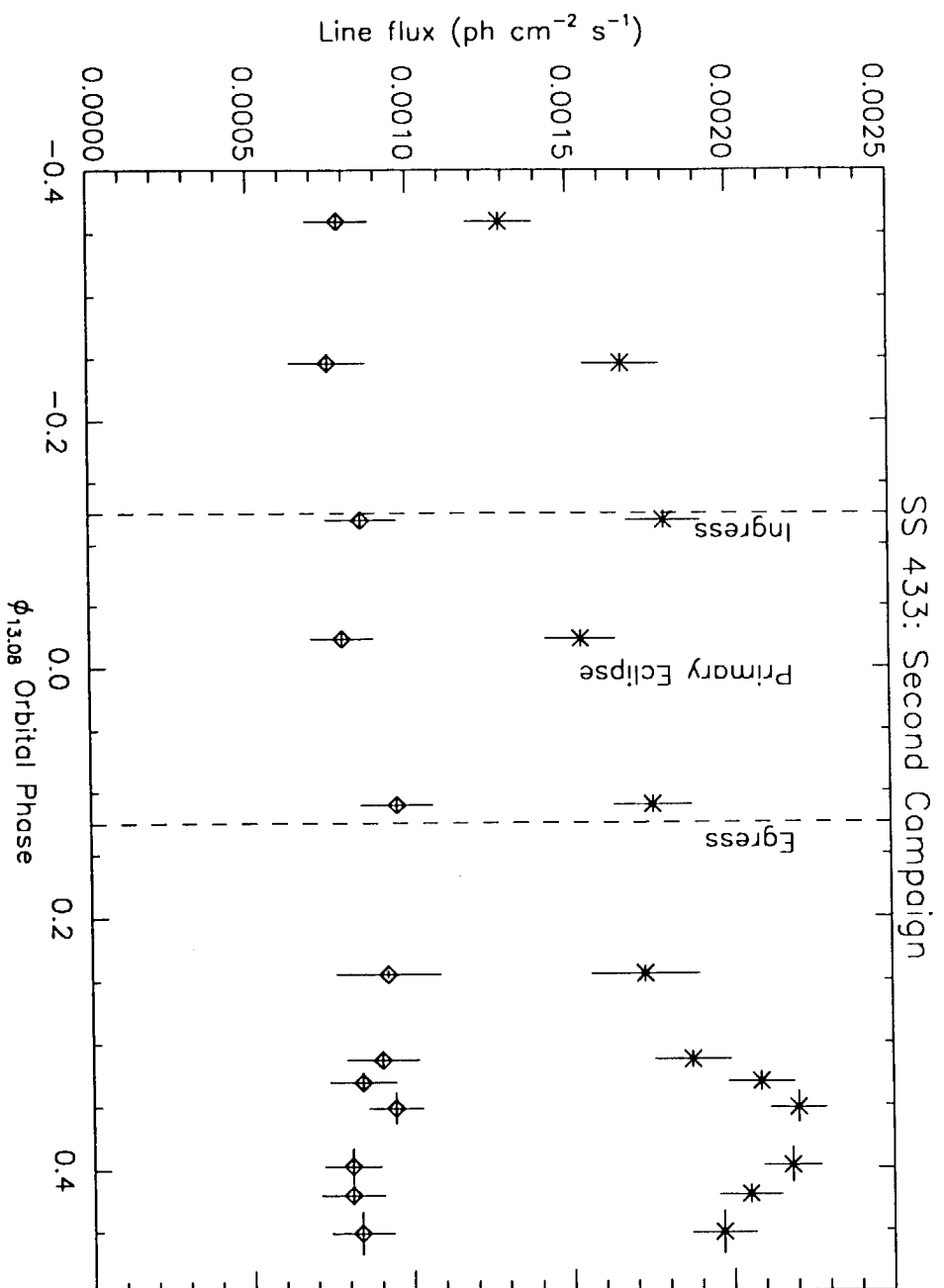


Fig 6c

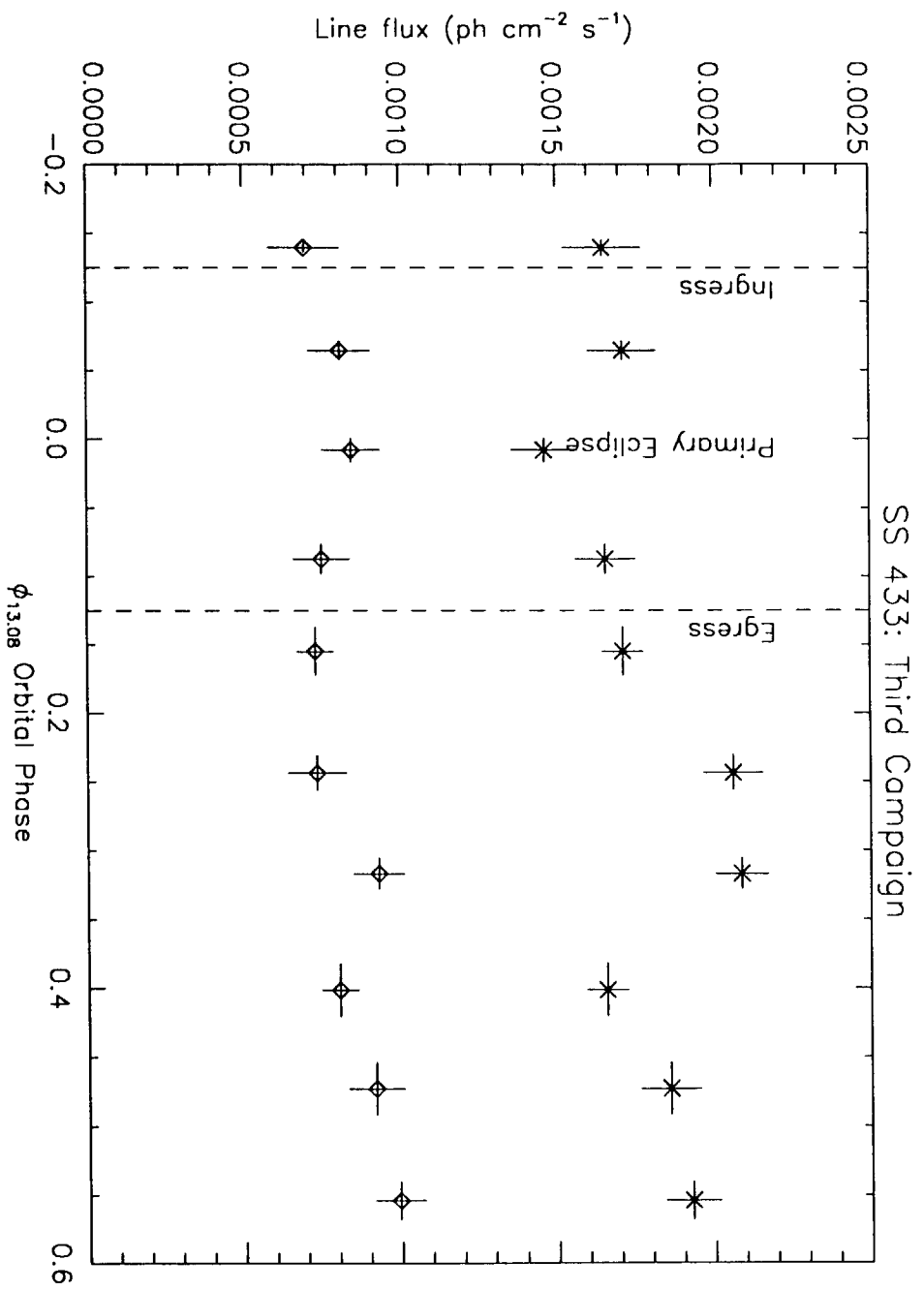


Fig 6d

SS 433: Entire Dataset

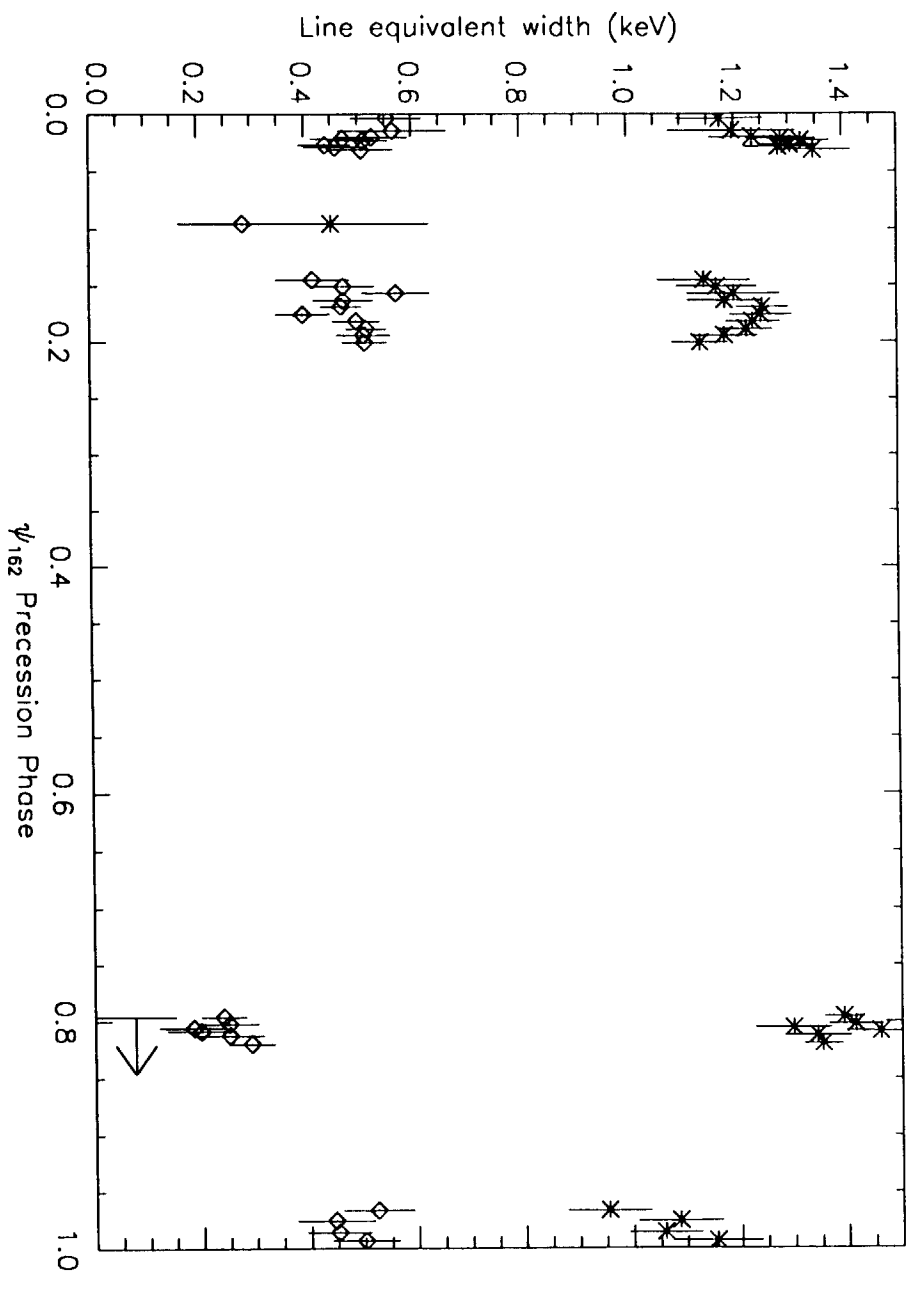


Fig 7a

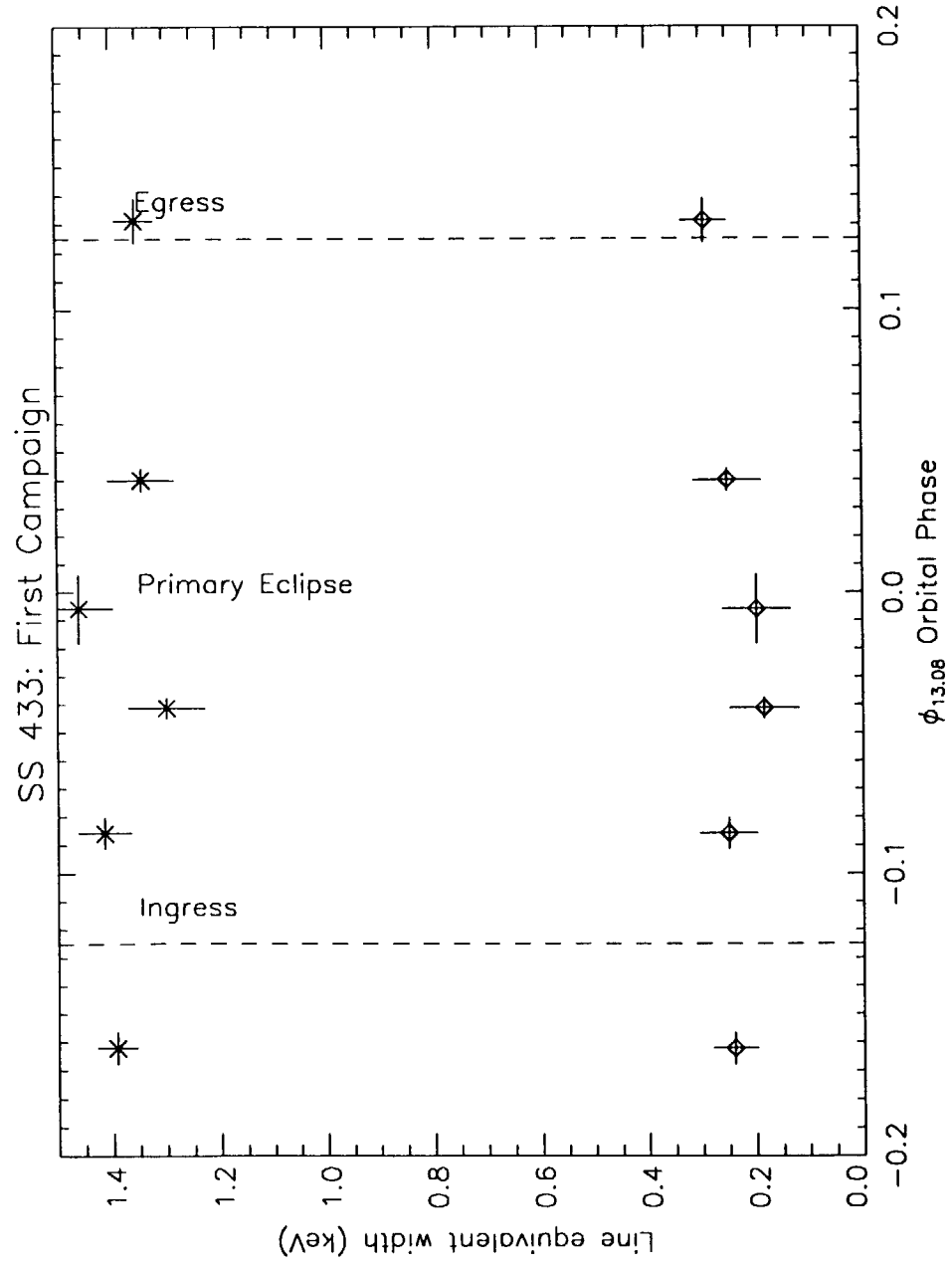


Fig 76

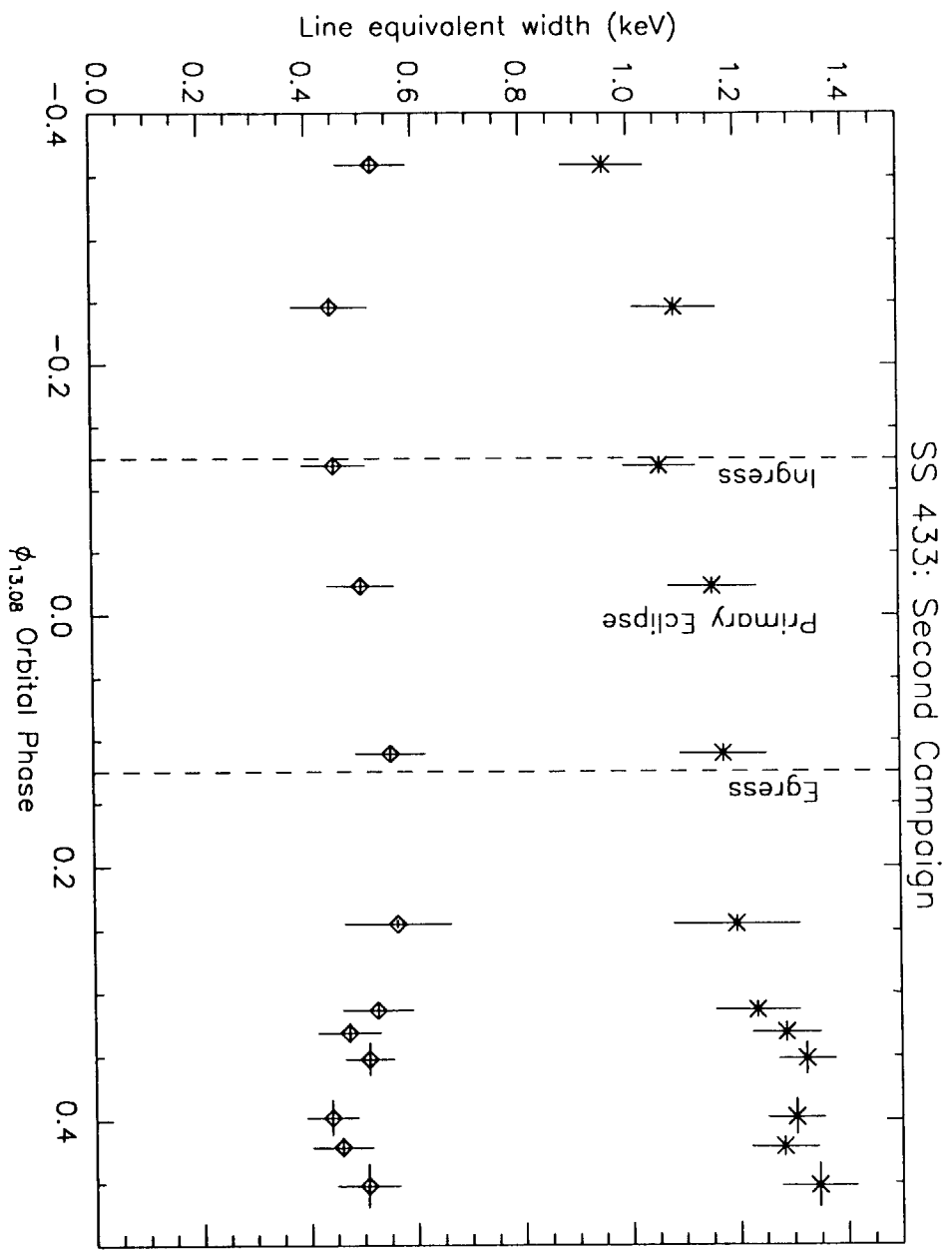


Fig. 7c

SS 433: Third Campaign

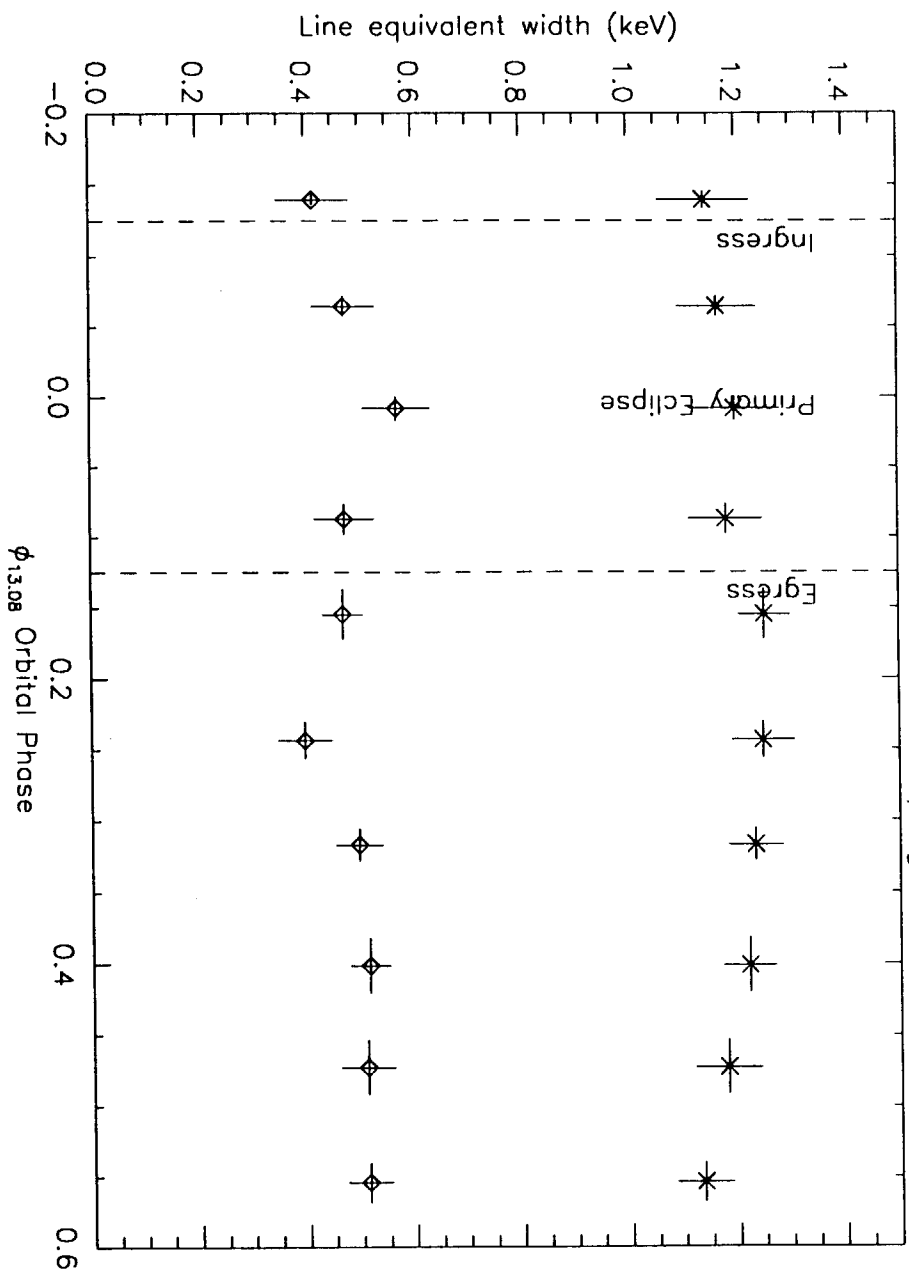


Fig 7d

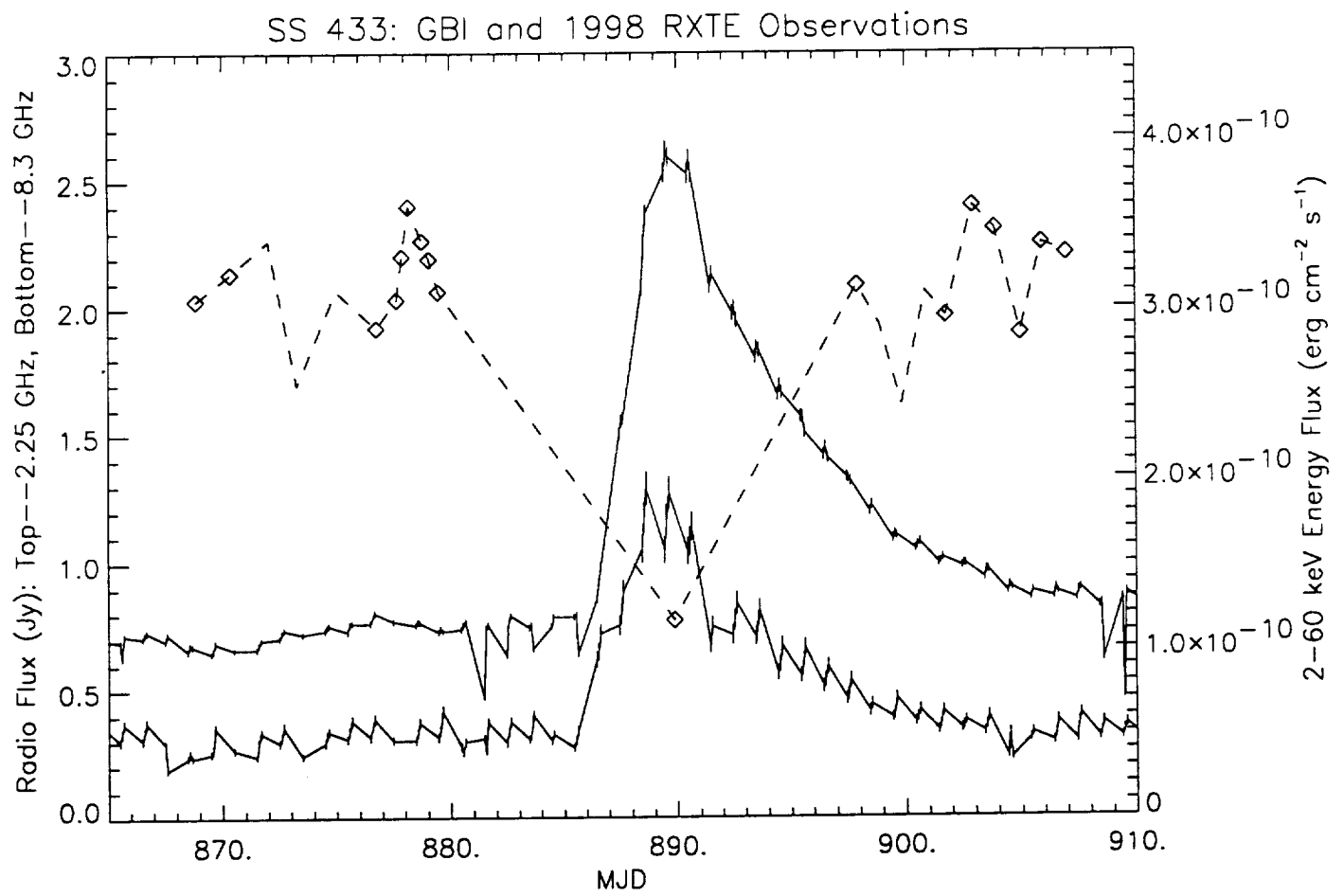


Fig 9

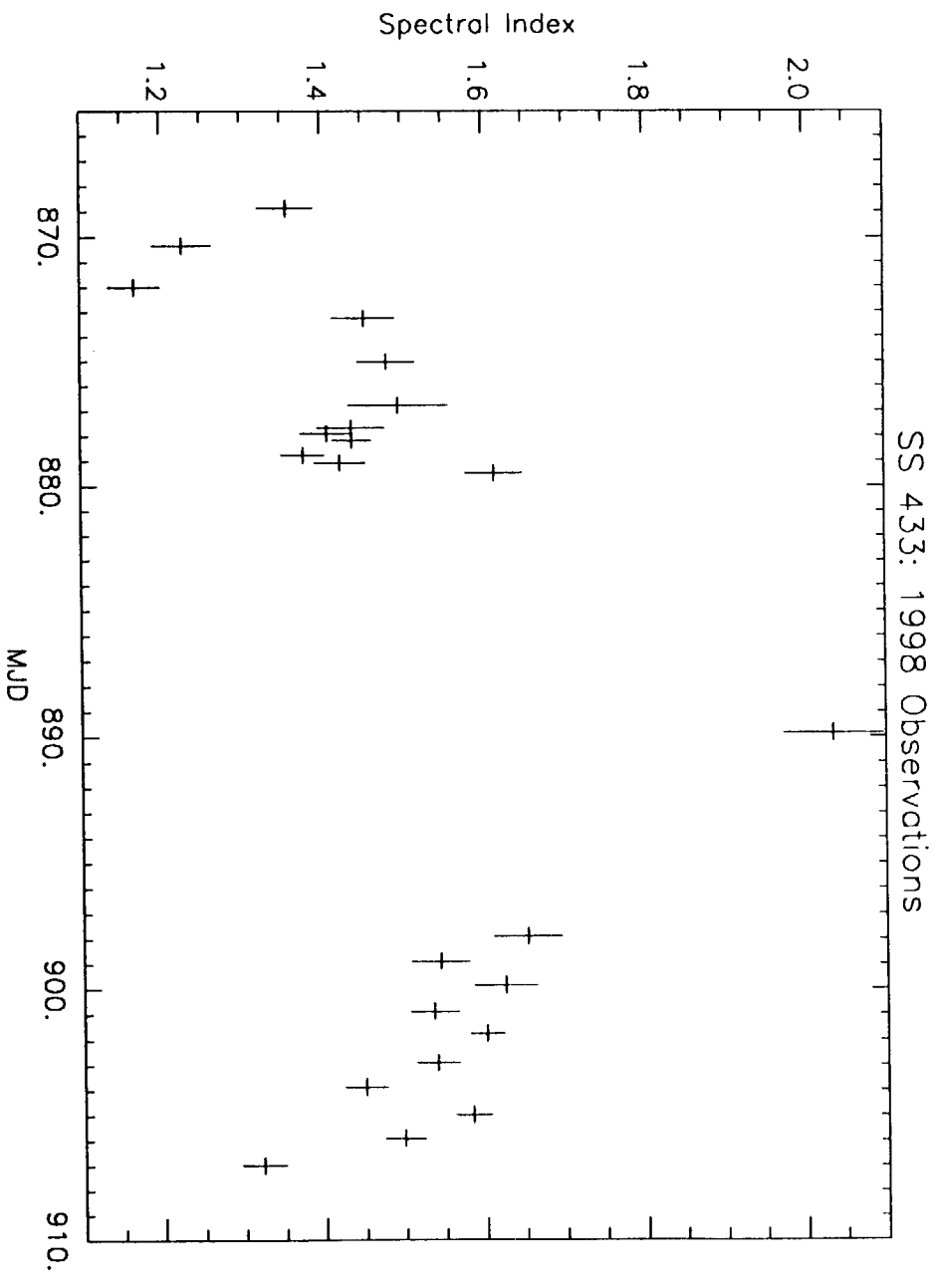


Fig 10



CENTER FOR ASTROPHYSICS AND
SPACE SCIENCES (CASS) 0424

9500 GILMAN DRIVE
LA JOLLA, CALIFORNIA 92093-0424

October 18, 1999

ONR, San Diego
4520 Executive Drive
Suite 300
San Diego, CA 92121-3019


REFERENCE: Grant No. NAG5-7643
Dr. David L. Band, Principal Investigator

SUBJECT: Final Technical Report

Enclosed is the final technical report for the project entitled "SS 433's High Energy Spectrum". Submitted in accordance with agency requirements.

If you have any further questions please call Bobbie Velasquez, Contract and Grant Officer, UCSD Contract and Grant Administration at 619/534-0242, email: bvelasquez@ucsd.edu

Sincerely,

Caroline Danmeier 
CASS
Administrative Specialist
(619) 534-1406
cdanmeier@ucsd.edu

cc: Jean Swank, Technical officer, NASA/GSFC
NASA - CASI
Dr. David L. Band
B. Velasquez OCGA
file